Development of a Thin Film Photoanode based on Titanium Dioxide for Photo-electrochemical Water Splitting

Von der Fakultät für Mathematik und Naturwissenschaften der

Carl von Ossietzky Universität Oldenburg zur Erlangung des Grades und Titels

Doktor der Naturwissenschaften

(Dr. rer. nat.)

von Herrn

Dennis Berends

(geboren am 20.09.1989 in Leer, Ostfriesland)

angenommene Dissertation.

Kurzfassung

Schwarzes Titandioxid (B-TiO$_2$) hat sich als vielversprechendes Material für die Erzeugung von grünem Wasserstoff und die damit verbundene Langzeitspeicherung von Energie durch photoelektrochemische Wasserspaltung erwiesen. Bisher konzentrierte sich die Forschung hauptsächlich auf die Herstellung von Nanopartikeln, während Dünnschichttechnologien für B-TiO$_2$ nur selten untersucht wurden. Vor diesem Hintergrund ist es das Ziel dieser Arbeit ein innovatives Sputterverfahren zur Synthese von B-TiO$_2$-Dünnschichten zu entwickeln. Eine Besonderheit des vorgestellten Verfahrens ist die völlige Unabhängigkeit von Wasserstoff als reduzierendes Prozessgas, der in herkömmlichen Verfahren als essentieller Bestandteil fungiert. Die hergestellten Dünnschichten zeigen gegenüber vergleichbaren Materialien aus der Literatur eine erhöhte Stromdichte während der Wasserspaltung auf, was auf eine gesteigerte Wasserstoffproduktion hinweist.

Die Abscheidung dieser B-TiO$_2$-Dünnschichten wird durch die Kombination zweier unterschiedlicher Sputtermethoden erreicht. Zum einen wird der Sauerstoffpartialdruck während des Prozesses in der Sauerstoffhysterese konstant gehalten. Zum anderen wird die auf die beiden Titantargets zugeführte Leistung asymmetrisch verteilt. Durch Variation der Leistungsverteilung können entscheidende Eigenschaften, wie die Lichtabsorption und die elektrische Leitfähigkeit der gesputterten Schichten präzise eingestellt werden.

Besonders hervorzuheben ist die gezielte Steuerung der Menge an Sauerstoffdefektstellen, die für die Steigerung der Wasserspaltungsreaktionen und somit der gemessenen Stromdichte von zentraler Bedeutung sind. Es wird gezeigt, wie sich diese Menge in Abhängigkeit von den Prozessparametern verändert. Mit diesen Erkenntnissen kann ein Regime im Parameterraum gefunden werden, das eine ideale Kombination aus der Anzahl der Sauerstoffdefektstellen und der sich einstellenden Änderung der Bandstruktur des B-TiO$_2$ Halbleiters hinsichtlich der photoelektrochemischen Wasserspaltung ergibt.

Aufgrund der asymmetrischen Leistungsverteilung innerhalb des Prozesses ergibt sich ein inhomogenes Schichtwachstum der Dünnschichten. Es wird gezeigt, dass die resultierende Schicht aus mehreren Lagen alternierender amorpher und kristalliner Phasen besteht. Dieser Schichtstapel ist sowohl für die optoelektronischen Eigenschaften als auch für die photoelektrochemische Wasserspaltung günstig. So kann für diese mehrphasige Probe während der Messung ein deutlich höherer Strom gemessen werden als für die einzelnen Phasen der Probe.

Die Ergebnisse dieser Forschungsarbeiten tragen nicht nur zur Weiterentwicklung von Dünnschichttechnologien bei, sondern zeigen auch vielversprechende Perspektiven für großtechnische, effiziente und zukunftsfähige Methoden der Materialentwicklung für die

photoelektrochemische Wasserspaltung auf. Die potenziellen Auswirkungen dieser Arbeit erstrecken sich auf den weiteren Bereich der erneuerbaren Energien und positionieren das entwickelte Verfahren als eine praktikable Lösung für die umweltfreundliche Wasserstoff-produktion. Insgesamt trägt diese Arbeit dazu bei, einen weiteren wichtigen Schritt in Richtung kommerzieller B-TiO$_2$ basierter photoelektrochemischer Systeme zu machen.

Abstract

Black titanium dioxide (B-TiO$_2$) has emerged as a promising material for the production of green hydrogen and associated long-term energy storage through photoelectrochemical water splitting. To date, the focus of research has been mainly on the production of nanoparticles, while thin film technologies for B-TiO$_2$ have rarely been investigated. In this context, the aim of this work is to develop an innovative sputtering process for the synthesis of B-TiO$_2$ thin films. A special feature of the process presented is its complete independence from hydrogen as a reducing process gas, which is an essential component in conventional processes. The thin films produced demonstrate an increased current density during water splitting compared to similar materials in the literature. This indicates an increased hydrogen production.

The B-TiO$_2$ thin films are deposited using a combination of two sputtering methods. First, the oxygen hysteresis is used to keep the oxygen partial pressure constant throughout the process. Second, the power applied to the two titanium targets is distributed asymmetrically. By varying the power distribution, key properties like light absorption and electrical conductivity of the sputtered layers can be precisely adjusted.

The control of oxygen defects is particularly noteworthy as it is central to increasing water splitting reactions and the resulting current density. It is shown how this quantity changes as a function of the process parameters. With these findings, a regime can be found in the system that leads to an ideal combination of the amount of oxygen defects and the resulting change in the band structure of the B-TiO$_2$ semiconductor with respect to photoelectrochemical water splitting.

The asymmetric power distribution within the dynamic process results in inhomogeneous layer growth of the thin films. It is shown that the resulting sample consists of multiple layers of alternating amorphous and crystalline phases. This layer structure is favourable for both the optoelectronic properties and the photoelectrochemical water splitting. Thus, a significantly higher current can be measured for the laminated sample than for the individual phases of the sample.

The results of this research not only contribute to the further development of thin film technologies, but also provide promising prospects for large-scale, efficient and future-oriented materials development methods for photoelectrochemical water splitting. The potential impact of this work extends to the wider field of renewable energy and positions the developed process as a viable solution for environmentally friendly hydrogen production. Overall, this work contributes to taking another important step towards commercial B-TiO$_2$ based photoelectrochemical systems.

Contents

1.   Introduction

1.1 Motivation

In recent years, Europe has found itself in a severe energy crisis. It faces the difficult task of dealing with geopolitical tensions, dwindling fossil fuel reserves, environmental concerns and the urgent need to secure a sustainable and resilient energy future.[1,2] Therefore, the need to utilise renewable energy generation methods has grown constantly.[3,4] In addition to independent power and heat generation, there is another urgent need for sustainable energy sources. This relates to the greatest crisis of our time, man-made climate change. The global climate crisis has become one of the most pressing challenges of our time, with far-reaching consequences for the interconnected systems of water, energy and food.[5] This complex relationship, known as the water-energy-food nexus, is the cornerstone of societal well-being and environmental sustainability. The human-induced climate change has triggered disruptions in these critical sectors and fundamentally altered their dynamics. [6]

In the face of these challenges, innovative solutions are needed to mitigate the negative effects of climate change while improving resource efficiency. Photocatalytic materials have emerged as a promising tool to tackle the climate crisis and revolutionise the water-energy-food nexus.[7] These semiconductor materials harness the power of sunlight to drive chemical reactions. It offers a path to sustainable energy production and environmental remediation. By using semiconductors to convert solar energy into chemical energy, it becomes possible to produce clean fuels such as hydrogen and remove pollutants and greenhouse gases from the atmosphere and the environment.[8] The development of new, more efficient and less expensive materials plays an important role in meeting the ever-growing demand for them. To date, for example, there is still no commercially available photoelectrochemical cell for water splitting.[9] Fujishima et al. published the first paper on this topic back in 1972.[10] Using a titanium dioxide (TiO_2) thin film, they demonstrated the potential of photoelectrochemical water splitting. Since then, new materials have been intensively developed and researched. In addition to new materials, further research was carried out on TiO_2.[11–13] A particular focus was on increasing photo absorption. In addition to doping with other materials, further processes to reduce the band gap and improve photoelectrochemical activity were explored.[14–16]

In 2011, Chen et al. published a process for hydrogenated TiO_2. The resulting black layers are called black TiO_2 (B-TiO_2) due to their highly enhanced solar absorption.[17] To do this, they subjected crystalline nanoparticles to treatment with hydrogen. The outer nanometres of the particle became amorphous and highly absorbent to light, while the core remained

crystalline. The entire particle had a black colour after the treatment and showed an increased efficiency in photoelectrochemical water splitting compared to untreated TiO_2 nanoparticles. As this B-TiO_2 nanoparticle retained the excellent corrosion resistance properties of TiO_2, more research and investigations into further improvements, other fabrication methods and additional photocatalytic processes were undertaken in the following years.[18–20] One of these processes is the reduction of carbon dioxide (CO_2) and other greenhouse gases in order to reduce the increasing global warming.[21] Another area of application for the photocatalytic processes is drinking water treatment. While larger particles can be removed by simple filter systems, the filtering of pathogens and other organic pollutants is more complex. However, these can be destroyed by sunlight and corresponding photocatalytic materials, like B-TiO_2, making the water drinkable. This process is self-sufficient and can therefore be used wherever the sun shines.[8]

Photocatalytic materials not only decompose undesirable molecules or substances but can also store energy. Sunlight is used to photoelectrochemically split water to produce green hydrogen, i.e. without the emission of greenhouse gases.[22] This chemical energy storage is considered one of the best long-term options. In the northern regions of Europe, sunlight is scarce throughout the winter months.[23] This significantly limiting the capacity of photovoltaic systems to generate adequate electricity. Moreover, when calm and cloudy weather prevails, the two primary sources of renewable energy, wind and solar power, are unable to be harnessed. In order to avoid having to fall back on fossil fuels to fill the gap in the electricity supply, hydrogen can be converted into electricity by means of fuel cells.[24] In this way, hydrogen can also be used to replace fossil fuels in vehicles. While most cars can run directly on electricity energy from a battery, this technology is less suitable for heavy vehicles such as trucks or ships. For these vehicles, hydrogen could be a better option.[25] Hydrogen is also needed in industry. Ammonia production for example require extreme quantities of hydrogen.[26] In steel production, which is one of the main sources of CO_2 pollution, hydrogen can replace the required carbon as the reducing agent.[27] Green hydrogen can be used to make these processes emission-free.[28,29]

As mentioned above, up to now, there is no commercially available photoelectrochemical cell for water splitting. However, there are many important steps in this direction, such as the development of new efficient materials like B-TiO_2, but the production process can still be optimised. So far, there are mainly publications on B-TiO_2 nanoparticles. However, the use of nanoparticles is not suitable for effectively coating large areas. In industry, sputtering has established itself as an efficient and cost-effective method for this. Sputtering processes for producing B-TiO_2 thin films have been reported only to a limited extent. Those that do exist use hydrogen to create the increased water splitting activity. In production, hydrogen requires additional safety measures, including explosion protection.[30]

Moreover, the use of two reaction gases simultaneously presents a challenge as it renders the process unstable.[31] Thus, it is necessary to create B-TiO$_2$ thin film photoanodes that do not require hydrogen during production and demonstrate enhanced water splitting performance.

This work aims to study such a novel B-TiO$_2$ thin film. A comprehensive analysis of the electrical, morphological, optical and photoelectrochemical properties of the thin film can explain how the enhanced water splitting performance is achieved. In addition, the newly developed sputtering process for producing the thin films is not only impressive in its simplicity, but also demonstrates its scalability. In the search for sustainable energy solutions, the demonstrated ability to produce efficient B-TiO$_2$ thin films is therefore an important step towards more efficient and environmentally friendly green hydrogen production. The study of B-TiO$_2$ thin films will also lead to a better understanding of their electrochemical behaviour and provide insights for their development. This work is in line with global efforts to develop clean and renewable energy sources. The text highlights the potential of advanced materials to promote the field of photoelectrochemistry and promote the widespread adoption of solar water splitting technologies.

1.2 Objective and Structure of the work

As part of renewable energy research, this work addresses the need for efficient and sustainable materials to produce green hydrogen using solar energy. A novel B-TiO$_2$ thin film photoanode has been developed for this purpose. This is characterised by a significantly increased water splitting performance compared to pristine TiO$_2$. Additionally, the production process is simplified as no hydrogen is required. The objective of this work is to study in detail how the increase in performance is achieved.

In order to gain an optimal understanding of the properties of the thin film, it is essential to first understand the deposition process in its entirety. This subject is thoroughly discussed in **Publication I** (chapter 4). To this end, experimental measurements and optical modelling are employed to study the optoelectronic and morphological properties of the B-TiO$_2$ thin film, with the objective of understanding the enhanced activity observed during photoelectrochemical water splitting.

Having discussed the deposition process in detail, the next question is to identify the physical factors that underlie the observed increase in optical absorption and electrical conductivity. Various measurement methods and models are used to answer this question. In

particular, the number of defect states and the band structure were analysed. This is discussed in detail in Publication II (chapter 5).

Due to the asymmetry of the novel sputtering process, it is anticipated that the film growth will be inhomogeneous. Therefore, it is crucial to identify whether this inhomogeneity is beneficial or detrimental to the objective of photoelectrochemical water splitting. To achieve this, a comprehensive morphological analysis of the film is conducted to understand the film growth. Subsequently, to identify whether the existing layer structure leads to an increase in water splitting performance, detailed photoelectrochemical measurements are carried out. This study is presented in **Publication III** (chapter 6).

The thesis is divided into several chapters. After introducing the topic in Chapter 1, Chapter 2 deals with the fundamentals and state of the art of bipolar reactive magnetron sputtering, black titanium dioxide and photoelectrochemical water splitting. Chapter 3 contains a brief summary of the three scientific publications produced in the course of this work, including the main results, analyses and conclusions. The accepted manuscripts are presented in Chapters 4, 5 and 6. Finally, in Chapter 7 places the individual publications in the wider context of the work, summarises the dissertation and draws conclusions.

2.   Fundamentals and State-of-the-Art

2.1 Bipolar Reactive Magnetron Sputtering

Developments in the field of physical vapour deposition (PVD) for the deposition of thin films have evolved from traditional sputtering processes to advanced techniques such as bipolar reactive magnetron sputtering. At its core, sputtering involves the detachment of atoms from a surface by the impact of high-energy particles, typically ions of an inert gas such as Ar^+. By applying a high voltage potential between the target and a counter electrode, usually the chamber wall, the inert gas introduced is converted into a plasma and the necessary ions are formed. Their energy is largely determined by the potential difference between the target and the chamber wall in conjunction with the prevailing chamber pressure. The atoms released from the target are then deposited on a substrate. The sputtering yield, a key parameter defined as the number of sputtered atoms released per incident particle, depends on factors ranging from the properties of the target material to the characteristics of the incident particles, including their type, energy and angle of incidence.[32–34]

The introduction of magnetron sputtering represents a significant improvement over previous technique. Magnets are arranged strategically behind the targets to align their magnetic fields precisely with the surface of the target. This alignment effectively traps the electrons close to the target, enhancing ionisation and achieving a higher sputtering rate. In addition, the enhanced plasma ionisation by the magnetic fields allows the use of lower chamber pressures and voltages. This reduction optimises the ion potential, resulting in an increased deposition rate. The combination of the increased sputtering rate, the reduced scattering of the sputtered atoms with the working gas and the preservation of the directional properties to the substrate contribute synergistically to an improved coating quality and to higher deposition rates.[35–37]

There are two practical options for sputtering composite materials such as oxides or nitrides: direct sputtering of the desired composite target with inert or reactive gas, or sputtering from a metallic target using an additional reactive gas. The low conductivity of ceramics often makes direct current (DC) sputtering from a composite target impractical. Conversely, reactive sputtering of metallic targets facilitates the deposition of composite layers with controlled stoichiometry. The composition and properties of the resulting film can be precisely controlled by adjusting the ratio of reactive gas to sputtering gas. In addition, the sputtering rate in this scenario exceeds that which can be achieved by direct sputtering from a composite target.[38–40]

In reactive DC sputtering, however, the chemical reaction between the metal and the reactive gas takes place on the surface of the target. This target poisoning is an unwanted formation of a nonconductive layer on the metallic target, reducing sputtering rates and causing charge build-up and arc erosion.[41] Remedial measures include switching the power supply from direct current to high frequency (RF, 13.56 MHz), medium frequency (MF, 50 - 350 kHz) or pulsed operation. The non-permanent impact of charge carriers on the target facilitates the discharge of the accumulated charges. In RF and MF sputtering, the electrons oscillate due to the high-voltage alternating current (AC) power source and generate ionising collisions. However, the disadvantage of this approach is a noticeable reduction in the sputtering rate, which significantly affects the morphology of the sputtered layer.[42,43]

To prevent target poisoning and increase the sputtering rate, a bipolar mode can be implemented by introducing a second target into the process. Each target is attached to a separate magnet. The anode and cathode electrodes alternate periodically between the targets. This alternation effectively prevents charge carrier accumulation and mitigates target poisoning. The cathode, which is exposed to the bombardment of heavy ions, and the anode, which is cleaned by the impact of electrons, together produce a sputtered layer with fewer defects and eventually achieve a deposition rate comparable to that of metallic targets.[40,44,45]

A detailed description of the process developed as part of this thesis can be found in the first publication. The hysteresis occurring in reactive sputtering, which has not yet been mentioned in this chapter, is also discussed in detail there.

2.2 Photocatalytic water splitting

Photoelectrochemical water splitting is a promising approach to sustainable hydrogen production. Light energy is used to split water into hydrogen and oxygen. The Gibbs free energy required for this process is $\Delta G° = 237$ kJ/mol under standard conditions. The standard electrochemical potentials for the two half-cell reactions, $E°$ (H^+/H_2) and $E°$ (O_2/H_2O), are 0 V and +1.23 V (versus standard hydrogen electrode). The band gap of the semiconductor used must therefore be at least 1.23 eV. Taking overpotentials into account, like mass transport and kinetics, the band gap E_g should be at least 1.6 eV.[46] Furthermore, the conduction band minimum (CBM) and the valence band maximum (VBM) must span the electrochemical potentials $E°$ (H^+/H_2) and $E°$ (O_2/H_2O) in order to drive the hydrogen evolution reaction (HER) and the oxygen evolution reaction (OER) using the electron and holes generated under illumination.[47–49] Figure 2-1 illustrates the central elements of this process and the corresponding electrochemical reactions.
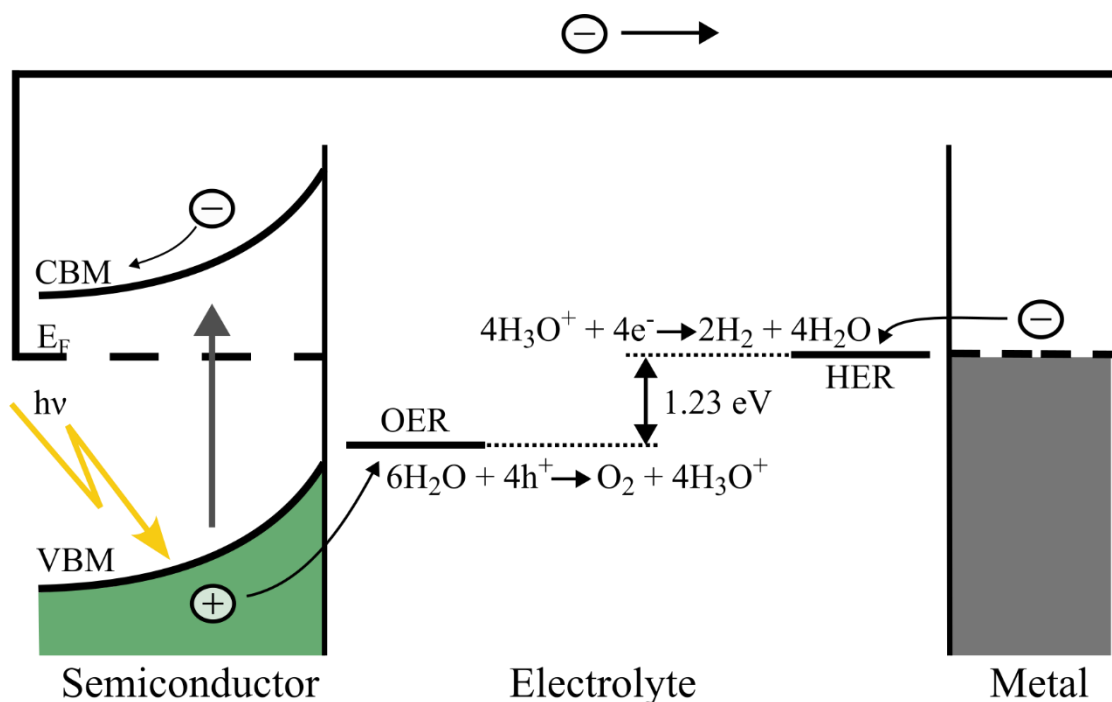
Figure 2-1: Schematic representation of the energy diagram of a photoelectrochemical cell. The cell consists of a n-type semiconductor photoanode and a metal cathode. To ensure charge equalisation, the two electrodes are connected by a cable and immersed in an electrolyte. The two equations represent the OER and the HER in an acidic electrolyte. For the semiconductor the valence band maximum (VBM), the Fermi level (E_F) and the conduction band minimum (CBM) are also indicated.

Like a conventional electrochemical cell (EC), a photoelectrochemical cell (PEC) requires two electrodes: an anode for the OER and a cathode for the HER. The difference with an

EC is that one or both of the metallic electrodes are replaced by semiconductor materials. When illuminated, the semiconductor absorbs photons with an energy at least equal to its band gap. The electrons are moved from the valence band to the conduction band, creating electron-hole pairs. This means that a PEC does not require an external voltage source, but generates the necessary voltage and charge carriers itself. However, an additional external voltage can lead to increased charge carrier transport and reduced recombination. Electrons flow from the photoanode to the cathode through an external wire. To complete the circuit, an electrolyte is used to facilitate ion conduction. Whether acidic, basic or neutral, the electrolyte allows the movement of protons and/or hydroxide ions, thus ensuring charge neutrality in the system.[46,50]

The driving force behind carrier separation is an in-build electrical field. In Figure 2-2 the band energetics of an n-type semiconductor/electrolyte contact under different circumstances is shown. At the interface between the photoanode and the electrolyte, charge transfer occurs until an equilibrium is reached (Figure 2-2A). This equalisation leads to the formation of a space charge zone within the semiconductor, also known as a depletion layer, in which the concentration of the majority charge carriers is lower than in the rest of the semiconductor (Figure 2-2B). Within this space charge zone, band bending occurs and a built-in electric field is created, allowing the photogenerated carriers to be separated and transported. This field can be amplified by an external voltage source.[51,52]
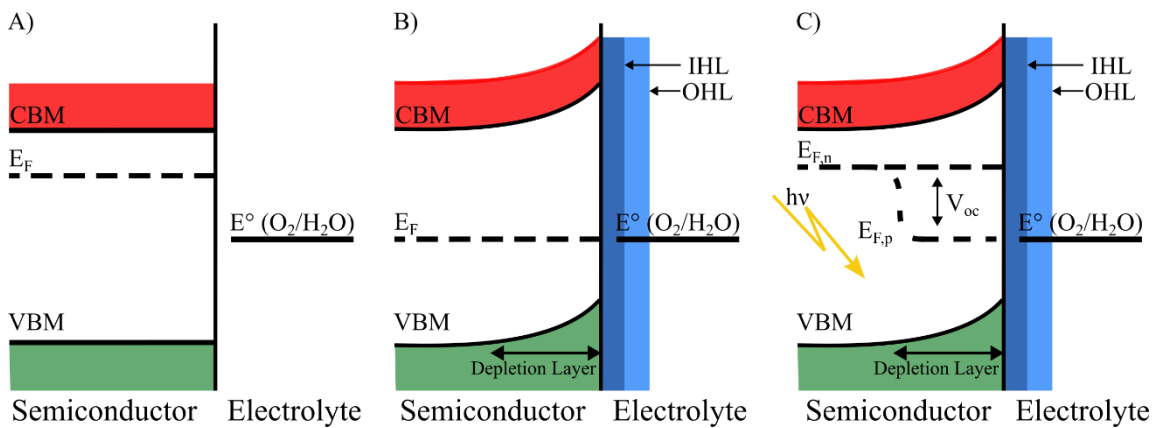
Figure 2-2: The band energetics of an n-type semiconductor/electrolyte contact showing the relationships between the electrochemical potentials $E°$ (O_2/H_2O), the CBM, the VBM, the Fermi level E_F, the electron quasi-Fermi level ($E_{F,n}$) and hole quasi-Fermi level ($E_{F,p}$) in three cases: A: before equilibration between the two phases; B: after equilibration under dark conditions; C: in quasi-static equilibrium under steady-state illumination. The voltage (V_{oc}) generated by the junction under illumination is given by the difference between $E_{F,n}$ and the electrochemical potential of the redox couple (O_2/H_2O for an n-type semiconductor and H^+/H_2 for a p-type semiconductor).

A layer is also formed between the semiconductor and the electrolyte, which in this case is negatively charged (Helmholtz layer). This layer is divided into an inner (IHL) and an outer Helmholtz layer (OHL). The thickness of IHL is determined by specifically adsorbed anions on the semiconductor surface, while the OHL refers to the shortest distance at which the ions are electrostatically adsorbed on the electrode surface.[53] The potential drops along this double layer. The density of surface states and the semiconductor properties influence this potential drop as well as the band bending and charge carrier density. When irradiated, the quasi-Fermi levels of the electrons $E_{F,n}$ and holes $E_{F,p}$ generate an open circuit photovoltage (V_{oc}), which is crucial for water electrolysis (Figure 2-2C). This is usually less than the band gap of the semiconductor. Photoelectrolysis of water is only possible when the V_{oc} is above 1.23 V.[54,55]

The water splitting reaction is an endothermic process characterised by a considerable activation energy and overvoltage.[56] It is therefore characterised by low activity. In addition, the kinetics of the multiple proton-coupled electron transfer is slow, especially in the case of water oxidation. This process is therefore often considered more critical than HER.[57] A detailed description of the single steps of both half-cell reactions are given in the equations 1-7:

$$2H_2O(l) + {}^* \rightleftarrows HO^* + H_3O^+ + e^- \tag{1}$$

$$HO^* + H_2O \rightleftarrows O^* + H_3O^+ + e^- \tag{2}$$

Anode

$$O^* + 2H_2O(l) \rightleftarrows HOO^* + H_3O^+ + e^- \tag{3}$$

$$HOO^* + H_2O \rightleftarrows O_2(g) + H_3O^+ + e^- \tag{4}$$

$$6H_2O \rightarrow O_2 + 4H_3O^+ + 4e^- \tag{5}$$

Cathode

$$4H_3O^+ + 4e^- \rightarrow 2H_2 + 4H_2O \tag{6}$$

Total

$$2H_2O \rightarrow O_2 + 2H_2 \tag{7}$$
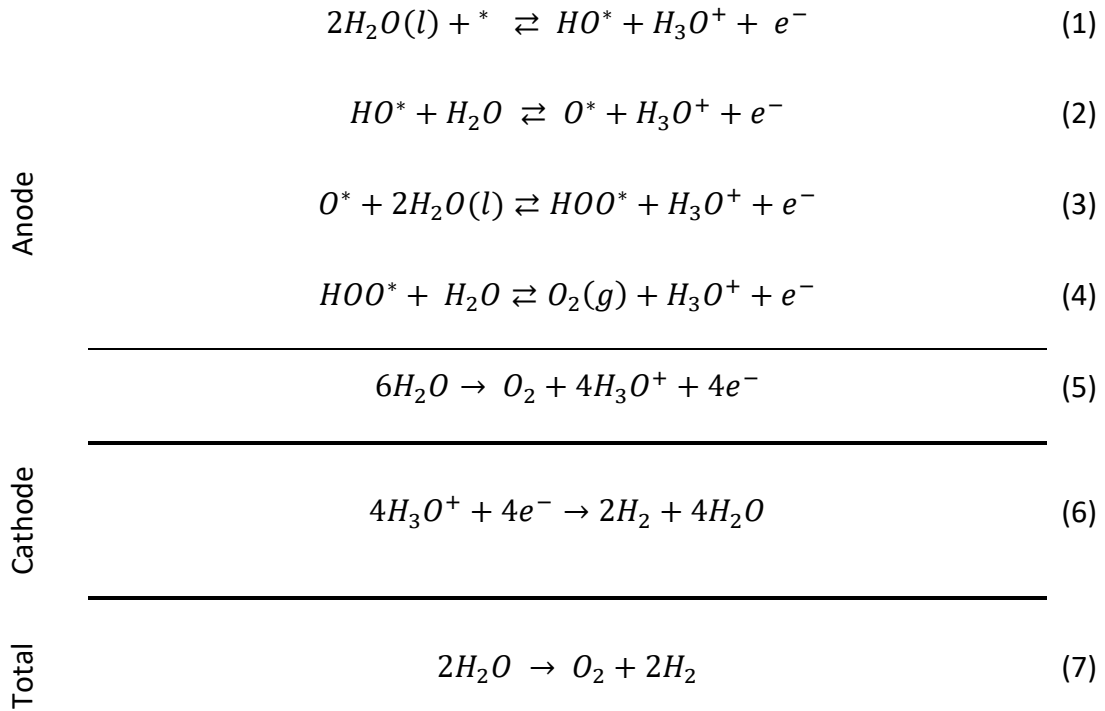
For the water oxidation, first, an H_2O molecule adsorbs on the surface (*), usually on an oxygen vacancy. Then an electron transfer takes place at the surface, oxidising the water molecule and forming O* species. This also releases two H_3O^+ ions and two electrons. O* reacts with another H_2O molecule to form the intermediate HOO*, releasing another H_3O^+ ion and an electron. Finally, gaseous O_2 is formed from the HOO*, together with an H_3O^+ ion and an electron. At the cathode, four hydronium ions then react with four electrons to form four gaseous hydrogen molecules (H_2) and four water molecules.[58]

2.3 Black Titanium Dioxide

Titanium dioxide (TiO_2) nanomaterials have been widely developed in the last five decades for photoelectrochemical processes like water splitting. However, the inherent limitation of pure TiO_2 phases lies in their wide band gap (3- 3.4 eV), which limits the absorption of solar energy mainly to the ultraviolet region. Many strategies have been explored to overcome this obstacle. One of the most important approaches is the doping of TiO_2 to reduce the band gap. This line of research has led to the development of intrinsic doping, such as the introduction of oxygen vacancies (VOs) and the formation of Ti^{3+} centres in the TiO_2 lattice. [59]

The synthesis of these TiO_2 layers involves high temperature treatments in various reducing atmospheres (e.g. vacuum, Ar, H_2/Ar and pure H_2). The resulting TiO_{2-x} can be grey, blue, brown or black depending on the specific conditions. The colouration is attributed to different concentrations of Ti^{3+} and VOs. A higher degree of defect density results in "darker" TiO_2 powders.[60–62]

In 2011, Chen et al. introduced the concept of B-TiO_2 nanomaterials for photocatalysis. In this approach, stoichiometric anatase TiO_2 is transformed into defect-rich nanocrystals by thermal treatment at 200 °C under high H_2 pressure. However, the core of the nanocrystals remains crystalline and the defects only occur in the outer few nanometres. The shape is therefore known as core-shell structure. These B-TiO_2 nanomaterials showed enhanced visible light absorption and superior photocatalytic activity for H_2 generation, especially when a Pt cocatalyst was incorporated.[17,63]

The improved performance of B-TiO_2 is attributed to an increased light absorption due to lattice disorder and H doping. This introduces electronic states that reduce the optical band gap to 1.54 eV and result in a significant narrowing of the valence (VB) and conduction band (CB).[64,65]

In addition to the enhanced light absorption, several other positive effects contribute to the improved hydrogen evolution. This includes the increased separation and transport of holes and electrons, along with the creation of more oxidation or reduction reactions sites at the surface. In particular, the presence of defects such as Ti^{3+}, VOS, Ti-OH and Ti-H groups increases the photocatalytic activity. These oxygen vacancies could introduce localized states in the bandgap and act as trap centres, significantly decreasing the electron-hole recombination while increasing the light absorption.[20,66–68]

Many applications beyond water splitting have been reported for B-TiO_2. These include nanoarchitectures for efficient photocatalytic processes,[59,69] carbon B-TiO_2 for dye-

sensitised solar cells,[70] B-TiO$_2$/graphene oxide nanocomposites for solar desalination and steam generation,[71,72] and B-TiO$_2$ nanotubes for electrochemical wastewater treatment.[73,74] In addition, B-TiO$_2$ has been used to improve the capacity and performance of lithium-ion batteries.[75,76] B-TiO$_2$ also shows promise for photothermal therapy of bone tumours and other cancer treatments.[77–79]

Various synthesis techniques have been used to produce B-TiO$_2$ nanoparticles, including hydrogenation,[80,81] thermal treatment in different atmospheres,[82,83] ionothermal processes,[84] microwave induced plasma,[85] plasma assisted methods,[86,87] magnesium reduction and NaCl-AlCl$_2$ salt melting.[88,89] Thin film technologies such as sputtering are rather rare. However, a convenient and cost-effective synthesis method is still required for widespread practical application.[69,90,91]

3. Overview of the Publications submitted in the framework of this thesis

3.1 Publication I

Title: Effect of asymmetric power distribution in bipolar reactive sputtering on the optoelectronic and microstructure properties of titanium dioxide for solar water splitting

Authors: Dennis Berends, Patrick Schwager, Kai Gehrke, Martin Vehse, Carsten Agert

Contribution: Conceptualization, Formal analysis, Investigation (except HRTEM measurements), Methodology, Validation, Visualization, Writing – origin draft, Writing – review & editing

This paper describes in detail the newly developed asymmetric, bipolar reactive magnetron sputtering method. The special feature lies in the combination of two different methods. Firstly, the power applied to the two titanium targets is distributed asymmetrically. This distribution is called duty cycle (DC) and leads to different removal rates on the respective targets. The second aspect, which is crucial for the new asymmetric bipolar reactive magnetron sputtering process, is the phenomenon known as oxygen hysteresis. In this context, oxygen hysteresis refers to the dynamic, non-linear behaviour of the oxygen partial pressure observed in the system when the oxygen flow is varied. In this new process, the oxygen partial pressure is deliberately kept at a certain level within this hysteresis during the sputtering process. This controlled pressure within the oxygen hysteresis plays a crucial role in influencing the resulting properties of the B-TiO$_2$ thin films.

The research results indicate that, under a certain process condition, the sputtered B-TiO$_2$ layers exhibit an enhanced current during photoelectrochemical water splitting. This condition is at a specific DC of 75% (to 25%) of the total 8 kW used in combination with an oxygen partial pressure of $16 \cdot 10^{-6}$ mbar

3.2 Publication II

The improved properties exhibited by the novel B-TiO$_2$ film compared to pure TiO$_2$ films are investigated in detail. The underlying physical mechanisms responsible for these improvements are explored. Through a combination of optical modelling (Extended Drude and O'Leary-Johnson-Lim models), dark conductivity measurements and X-ray photoelectron spectroscopy (XPS), two distinct properties of the thin films were identified as key contributors to their superior performance.

The first notable observation is the evolution of Ti^{3+} states within the material up to DC = 75%. An increase in the proportion of Ti^{3+} states is observed, and interestingly, these states show a direct correlation with the increased photoelectrochemical water splitting activity of the thin film. Above 75% DC, however, the proportion of Ti^{3+} states stagnates. At the same time, this increase in the energy distribution results in a further decisive change in the properties of the thin film. Due to the formation of new energetic states, the band tails of the valence and conduction bands penetrate deeper into the band gap. This change contributes to increased light absorption and an increase in the electrical conductivity of the thin film. However, the photoelectrochemical activity decreases again for DC > 75%.

3.3 Publication III

Title: Analysis of the Inhomogeneous Growth of Sputtered Black TiO_2 Thin Film

Authors: Dennis Berends, Patrick Schwager, Kai Gehrke, Martin Vehse, Carsten Agert

Contribution: Conceptualization, Formal analysis, Investigation (except TEM and EDX measurements), Methodology, Validation, Visualization, Writing – origin draft, Writing – review & editing

The investigation of the growth and composition of the thin film is the focus of the third work, which enables a differentiated understanding of the complex processes. During the sputtering process, the sample is moved several times in front of the two titanium targets, which leads to different material compositions due to the asymmetric energy distribution. The resulting layer stack therefore shows a repeating sequence of inhomogeneous layers. To unravel the complexity of this dynamic sputtering process, the dynamic process is converted into a static one. This transforms the sputtering process into a static process. In this way, every point during layer growth can be measured and analysed.

A fascinating result of this analysis is the formation of two distinct regions that are mainly sputtered, with a small but steady transition between them. The region in front of the target with lower energy leads to the deposition of crystalline, transparent but poorly conducting material. Conversely, amorphous, black and conductive material is deposited in the area in front of the target, which is operated at higher power. While the edge regions of the black area show the highest currents during photoelectrochemical water splitting, the dynamic sample shows a significantly improved water splitting activity. This astonishing phenomenon is attributed to an increased accumulation of charge carriers at the interface between amorphous and crystalline regions.

4. Publication I: Effect of asymmetric power distribution in bipolar reactive sputtering on the optoelectronic and microstructure properties of titanium dioxide for solar water splitting

4.1 Abstract

Titanium dioxide is one of the most commonly used materials for solar water splitting, because of its excellent corrosion resistance. However, its optoelectronic properties are not sufficient to achieve high solar to hydrogen conversion. It is known that the choice of deposition method has a great influence on the optoelectronic and structural properties of titanium dioxide.

Here we combine two different sputtering configurations and vary the process parameters to obtain thin films of black TiO_x. Bipolar magnetron sputtering from two metallic titanium targets is used in combination with an oxygen partial pressure control via a closed-loop residual gas monitoring system. The power distribution between the two targets in the bipolar sputtering mode is thereby varied from sample to sample, while the oxygen partial pressure remains constant. This causes one target to shift into the oxidic regime, while the other target shifts into the metallic regime. Because the metallic target has a higher sputter yield the process leads to off-stochiometric samples. These samples exhibit a broad-band absorption and an increased photoelectrochemical activity (up to five times) compared to samples without the modification of the power distribution. The results are discussed based on the optoelectronic and microstructural analysis of the thin films.

4.2 Introduction

The need for green hydrogen (H_2) is known for years and its demand is very likely to rise in the near future [29,92]. Hydrogen can be used not only to power vehicles, but also for a large-scale long-term storage of renewable energy from fluctuating solar and wind sources [93–95]. One way to produce green hydrogen is to split water in a photoelectrochemical cell (PEC) [47,57,96]. Within the PEC sunlight is absorbed creating energetic electrons used in the hydrogen evolution cycle. To realize such a cell and make it commercially available, different configurations and materials for the photoactive electrodes have been

investigated [58,97–100]. The goal is to achieve a solar-to-hydrogen conversion efficiency of ≥10% together with a long lifetime and to be financially competitive with other, non-green H2 production paths [101–103]. However, no such viable combination has yet been found [104]. Titanium dioxide (TiO_2) is the first and most studied material for a photoanode in a PEC [10,105–110]. It is long-term stable, earth-abundant and corrosion resistant [111–115]. However, its band gap is too wide (3.2 eV) for efficient solar water splitting [55,116,117].

To increase the water splitting performance various approaches have been pursued. For example, the influence of the different polytypes (anatase, rutile, brookite) has been investigated [108,118]. While brookite is rarely considered for solar water splitting, anatase is known to achieve higher efficiencies than rutile. However, a feasible mixture of both phases can enhance the photoelectrochemical activity even further [108,119]. Another approach is to create non-stoichiometric TiO_x, in which the partial removal of oxygen atoms creates defects that lead to increased light absorption and conductivity of the layers. Black titanium dioxide is one example of such an approach [17,120]. Through hydrogenation of stochiometric titanium dioxide a defect rich layer can be created, which leads to an improved photoelectrochemical water splitting performance [68,121]. Further efforts to reduce the band gap of TiO_2 have been made by incorporation of ions into the lattice [120,122–124].

With the right choice of TiO_2 deposition technique, any or all of the previously mentioned attempts can be addressed. Reactive DC magnetron sputtering from a metallic titanium target is such an industrially proven technique [125–127]. Recently, there have been efforts to transfer the industrially used automated sputtering process combined with computerized control to laboratory scale to achieve greater versatility [128]. This process allows fine tuning of the properties of TiO_2 thin films by precisely controlling the deposition parameters. The substrate temperature can be used to influence the crystal structures of the layers [126,129]. Non-stoichiometric layers can be deposited by tuning the target power as well as the relative proportion of the reactive gas oxygen (O_2) in the argon (Ar) sputtering gas, which can affect the optoelectronic properties of the samples [12,130]. However, reducing the oxygen partial pressure also results in a non-linear increase of the sputter rate. An increase in oxygen partial pressure in the same range leads, however, to a different, non-linear decrease of the sputter rate. This phenomenon is called hysteresis [111,131,132]. At partial pressures close to zero, the deposited layers exhibit metallic properties. For high partial pressures, by contrast, the targets are completely poisoned and the deposited layers are stoichiometric TiO_2. However, at partial pressures between those two regimes, non-stoichiometric TiO_x layers can be produced. TiO_x layers with an O_2 deficit exhibit a reduced band gap and increased conductivity [133,134].

The common technique uses sputtering from one target. However, using two targets has an advantage compared to the use of one target. During reactive sputtering from one target, this electrode remains as the anode and is poisoned through the sputter process. In addition, the chamber that acts as the cathode is coated with the sputtered insulating material. This can cause the problem of a disappearing anode, if the chamber and the target have the same potential [135]. By adding a second target, bipolar sputtering continuously switches both targets between anode and cathode during the sputter process. While one target acts as the cathode, its insulating layer on the surface is removed. Therefore, one pure target remains in the chamber and no disappearing anode problem occurs [31]. Since sputtering from two targets affects the deposition rate, the hysteresis noted above is also affected. Compared to single magnetron sputtering, the hysteresis curve in dual magnetron sputtering has a sharper transition from the metallic to the oxidic regime. In addition, the hysteresis occurs at higher oxygen flows [136]. Since there are many different modifications of sputter deposition, a combination of two of these can result in improved or even new materials [137,138].

In this work, we report on an improved configuration for bipolar sputtering of non-stoichiometric TiO_2. Here, an asymmetric power distribution between two titanium targets is applied while the oxygen partial pressure is kept at a fixed value. We show that for a given oxygen partial pressure, the resulting sample shows an optimum in solar water splitting performance. These results are discussed along with the optical, electronic and microstructural properties of the deposited layer. Through these unique configurations during the deposition of the TiO_x photoanode, we understand our results to be a valuable step in further improving solar fuel technologies through a highly absorbent, conductive and photoactive TiO_x layer.

4.3 Materials and Methods

4.3.1 Thin Film Deposition

The TiO_x layers were produced by reactive sputter deposition using a Vistaris 600 in-line vacuum system (Singulus Technologies AG, Germany). The dual rotary magnetron was equipped with cylindrical metallic titanium targets (purity 3N) with a length of 600 mm and a diameter of 155 mm. The rotation speed was 10 rotations per minute for each target. The deposition was in a bipolar configuration with a low frequency switching of polarisation between the targets at 50 kHz, as describes by other authors [139]. Before starting the process, the chamber was pumped down to a base pressure of less than 10^{-5} mbar to avoid

contamination by residual gases. Further discussion of the negligible contamination by residual gases can be found in the supplementary part. The process pressure was in the range of 10^{-3} mbar. The process gas mixture consisted of Argon (purity 6N) and Oxygen (purity 5N5) controlled via mass flow controllers El-Flow select (Bronkhorst High-Tech B.V., Germany). While the Argon flow was kept constant at 300 sccm, the oxygen flow was continuously readjusted by a closed-loop partial pressure control, with the O_2 partial pressure measured by a mass spectrometer HPQ3 (MKS Instruments, USA) serving as the feedback parameter. With this method, it is possible to keep the oxygen partial pressure constant within the hysteresis during the deposition.

As noted above, the sputter rate shows a non-linear dependence on the oxygen partial pressure. A hysteresis between the increasing and decreasing oxygen flow can be seen in Figure 4-1a. As the reactive gas flow increases, the surface at the metallic target gets oxidized, causing the sputter rate to slowly decrease. At a certain flow, the oxidation leads to an abrupt drop of the sputter rate towards the sputter rate of a fully poisoned, e.g. ceramic target (Figure **4-1**a). This point of transition depends in particular on the sputter power and shifts to higher O_2 flows with higher power.
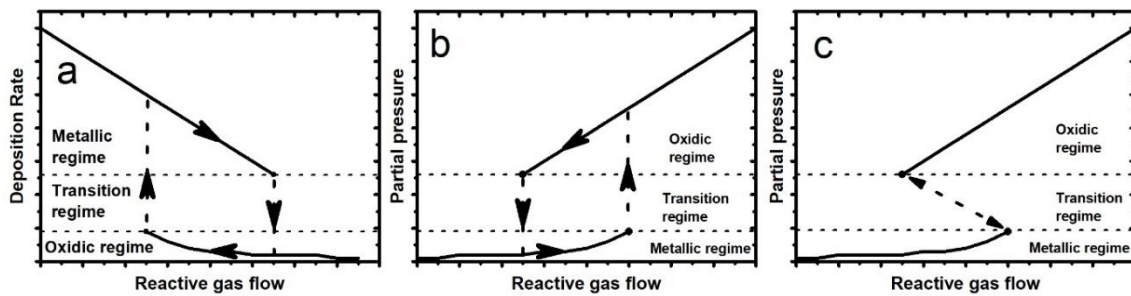

Figure 4-1: Theoretical behaviour of the a) deposition rate and b) the partial pressure by increasing the reactive gas flow as well as c) the possibility to get into the transition mode through partial pressure control

The decrease in the sputter rate leads to an increase in the oxygen partial pressure, as less oxygen is adsorbed on the oxidized target surface. During the transition, the regime changes from metallic to an oxidic, where the target is completely poisoned (Figure 4-1b). However, if the oxygen flow is reduced starting from the fully poisoned oxidic regime, the transition to the metallic regime occurs at a lower oxygen flow than in the increasing branch. The target remains oxidized because the sputter rate is too low to remove the poisoned layer from the target surface completely. Therefore, the oxygen flow must be reduced even further until the insulating layer on the target surface is partially removed and a rapid increase of the sputter rate occurs. At this point, the target surface can again adsorb more oxygen and the partial pressure of oxygen drops. The use of a closed loop feedback of the O_2 partial pressure allows the process to be stabilized in the transition regime (Figure

4-1c). The main advantage of controlling the partial pressure is the full control of the film stoichiometry, which can lead to a defined variation of material and layer properties while maintaining a high sputter rate [15,31,111,131,132,136,140,141].

The process temperature was set to 200 °C, samples were preheated for 12 minutes and 8 kW cumulative power P_c applied to both targets. The previously mentioned asymmetric power distribution can be expressed by the duty cycle dc, which determines the percentage of cumulative power Pc applied to one target, here target A (see Figure 4-2): $P_A = dc * P_c$. Therefore, the power applied on target B is $P_B = P_c - P_A$. For example, a duty cycle of 50% would mean a symmetrical power distribution of 4 kW for each target, while a duty cycle of 80% would mean 6.4 kW on target A and 1.6 kW on target B. The substrates were mounted on a carrier that passes the targets horizontally several times in the inline sputter process (Figure 4-2). As the substrate moves along the targets, the sputter rate has to be adjusted according to this dynamic process. The dynamic deposition rate (DDR) is calculated from $DDR = d * v/n$, where d represents the layer thickness, v the carrier speed and n the number of passes. More details on this parameter can be found elsewhere [142]. The produced layer thicknesses are in the range of 150 – 300 nm. The samples are prepared on 2.5 x 2.5 cm^2 soda-lime glass substrate for optical and electrical characterization and on a 10 x 10 cm^2 soda-lime glass substrate with a 200 nm silver electrode, previously deposited via electron beam evaporation (VTD Vakuumtechnik Dresden GmbH, Germany), for electrochemical measurements.
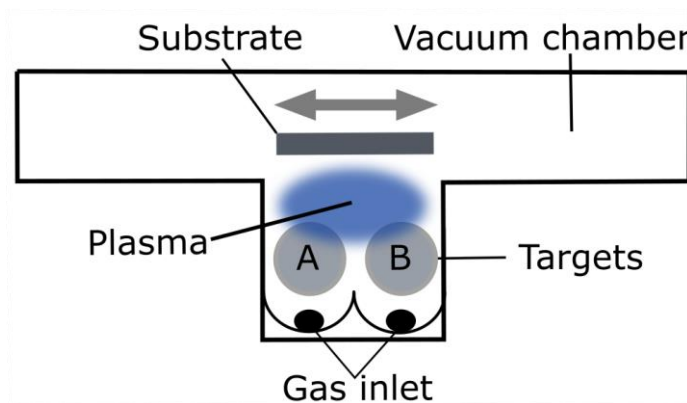

Figure 4-2: Simplified top-view of the process vacuum chamber with the horizontally moving substrate in front of the two targets A and B, the gas inlet and the plasma

4.3.2 Characterization Methods

The thickness d of the fabricated samples was measured with a Dektak 150 stylus profilometer (Veeco, USA). The sheet resistance $R_\square$ was measured using a Jandel RM3-AR four-point probe (Jandel Engineering LTD, UK). With the measured sheet resistance $R_\square$ and the thickness d, the resistivity ρ, $\rho = R_\square \cdot d$ was calculated. Optical measurements were performed in a Cary 5000 UV-Vis-NIR spectrophotometer using an integrating sphere (Agilent Technologies Inc., USA) with a wavelength range from 250 – 1500 nm. From transmission T and reflection R measurements, the absorption coefficient $\alpha = 2.303 \cdot \frac{A}{d}$ can be calculated with the absorption $A = 100 - T - R$ and the layer thickness d. Through the Tauc relation the band gap can be calculated via $\alpha h\nu = (h\nu - E_g)^n$, where $h\nu$ is the photon energy and E_g the optical band gap [116]. The constant n describes the electronic transition of the optical absorption, in this paper $n = 2$ was used for the calculations, describing an allowed direct transition [122,143]. For the structural analysis, Raman measurements were performed using a Senterra System with a 488 nm laser (Bruker Corporation, USA). Further measurements were carried out using a FEI Titan 80/300 G1 transmission electron microscope (TEM, Field Electron and Ion Company, USA), a Zeiss Neon 40 EsB crossbeam scanning electron microscope (SEM, Carl Zeiss Ag, Germany) and an Oxford INCA Energy 350 energy dispersive X-ray spectroscopy (EDX, Oxford Instruments, United Kingdom). Electrochemical characterization of the materials was performed with a VersaSTAT 4 potentiostat (Ametek scientific instruments, USA). A linear sweep voltammetry (LSV) in a three-electrode setup with an Ag/AgCl as reference electrode and a Platinum wire as the counter electrode (surface area of 83.68 cm^2) was used. The deposited TiOx layers served as the working electrode with an active area of 46.6 cm^2. 1M KOH (pH = 13) solution was used as the electrolyte. The scan rate of the LSV measurement was 50 mV/s. A halogen lamp (560W/m^2) was used for irradiation with visible light.

4.4 Results and Discussion

In this section we first present the parameter framework of TiO$_x$ deposition by bipolar reactive magnetron sputtering using oxygen partial pressure (OPP) control. We show the effects of the OPP and asymmetric power distribution on the deposition. Then we characterise the samples in terms of their optoelectronic and microstructural properties and the influence of these properties on the solar water splitting activity by linear sweep voltammetry.

4.4.1 Influence of oxygen partial pressure control and duty cycle on the deposition

The effect of oxygen flow on OPP during bipolar reactive sputtering at a 50% duty cycle is shown in Figure 4-3a. The oxygen flow was slowly and steadily increased from 0 to 100 sccm over a period of 200 s and then decreased back to zero in another 200 s. The black dots in Figure 4-3a show the resulting OPP during the increase of oxygen flow, while the green dots show the OPP measured while the oxygen flow was decreased. As described above, a hysteresis exists between the increasing and decreasing oxygen flow branches. In the decreasing oxygen branch in Figure 4-3a, there is no clear transition point between the oxidic and metallic regime. This phenomenon is often observed in reactive TiO_2 measurements and is related to the high reactivity of titanium with oxygen [15]. With these two measurements, the OPP control was calibrated and different OPP setpoints can be set. The setpoints are shown as triangles in Figure 4-3a. As can be seen, the OPP control loop stabilized the process within the hysteresis for a large number of OPP setpoints.

For further study, three OPP setpoints were chosen: $6 \cdot 10^{-6}$ mbar, $12 \cdot 10^{-6}$ mbar and $14 \cdot 10^{-6}$ mbar, respectively at the edge of the metallic/transition regime, in the middle of the transition regime and on the edge of transition/oxidic regime. In Figure 4-3a, these setpoints are shown as red dot, blue inverted triangle and magenta rectangle.
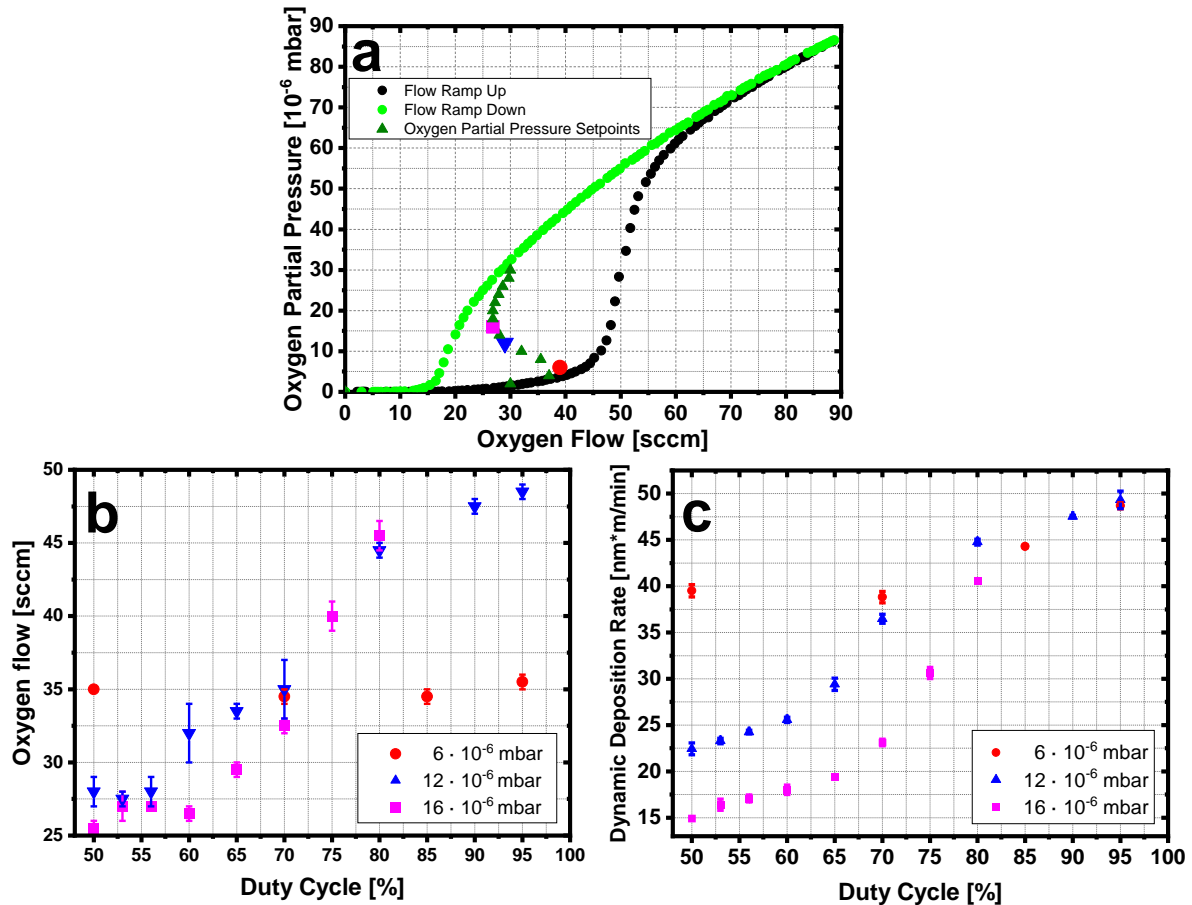
Figure 4-3: a) Constant increasing and decreasing oxygen flow (black and green line) and setpoints for different oxygen partial pressures with corresponding oxygen flow (blue dots) during bipolar sputtering with 50% duty cycle. The red, blue and magenta coloured dots represent the setpoints chosen for further investigation. b) Adjusted oxygen flow for different oxygen partial pressure by varying the duty cycle. c) Dynamic deposition rate for the three chosen oxygen partial pressure at different duty cycles.

For the next step, the influence of the increasing asymmetric sputter power distribution on the oxygen flow was investigated. As noted above, increasing the duty cycle shifts the power from target B to target A. Figure 4-3b shows the influence of this shift on the oxygen flow for three chosen oxygen partial pressures setpoints. The curves of $12 \cdot 10^{-6}$ mbar and $16 \cdot 10^{-6}$ mbar are comparable. At a duty cycle close to 50%, the oxygen flow does not change significantly. At a duty cycle over 60%, the oxygen flow increases. At a duty cycle of 80% this gradient decrease. Figure 4-3b indicates that target A has a higher sputtering yield due to the asymmetric power distribution, which is a consequence of an increased local power density. Therefore, this target is able to adsorb more oxygen. Hence, the oxygen flow has to be increased to maintain the partial pressure setpoint. However, target B has a lower sputter rate due to the lower power, so fewer oxygen atoms react at the surface and the oxygen demand decreases. Below 60% duty cycle, the asymmetric power

distribution is not large enough to affect the oxygen flow. The curve for $6 \cdot 10^{-6}$ mbar does not show any significant change with increased duty cycle.

Due to the variation of the duty cycle which goes along with a change in the oxygen flow, a change of the dynamic deposition rate is to be expected. This change can be observed in Figure 4-3c for the three oxygen partial pressures setpoints. The samples sputtered at a duty cycle of 50% have different gpd values, whereby the sample prepared at $6 \cdot 10^{-6}$ mbar has the highest value while the sample prepared at $16 \cdot 10^{-6}$ mbar has the lowest value. This can be explained by the initial choice of the oxygen partial pressure setpoints. For the metallic regime, $6 \cdot 10^{-6}$ mbar is chosen, while the partial pressures of $12 \cdot 10^{-6}$ mbar and $16 \cdot 10^{-6}$ mbar are in the transition and oxidic regimes, respectively. An increase of the duty cycle shifts target A to the metallic mode and increases its sputter rate. Figure 4-3c indicates that the influence of target A is not significant at a duty cycle close to 50%. Above a duty cycle of 60%, the influence of target A dominates, as the DDR and the oxygen flow increase drastically. At a duty cycle of more than 80%, the increase saturates and approaches the DDR of the $6 \cdot 10^{-6}$ mbar samples. At such a high duty cycle, target B has only a limited influence in the DDR due to the low power. The sample thicknesses can be seen in Figure S4-1 in the supplementary section. The range of the thicknesses is between 200 nm and 400 nm.

4.4.2 Optoelectronic Characteristics

Varying the duty cycle not only leads to changes in the DDR, but also influences the optoelectronic properties of the samples. Figure 4-4a shows the influence of the duty cycle on the band gap extracted from Tauc plots for two different OPP setpoints.
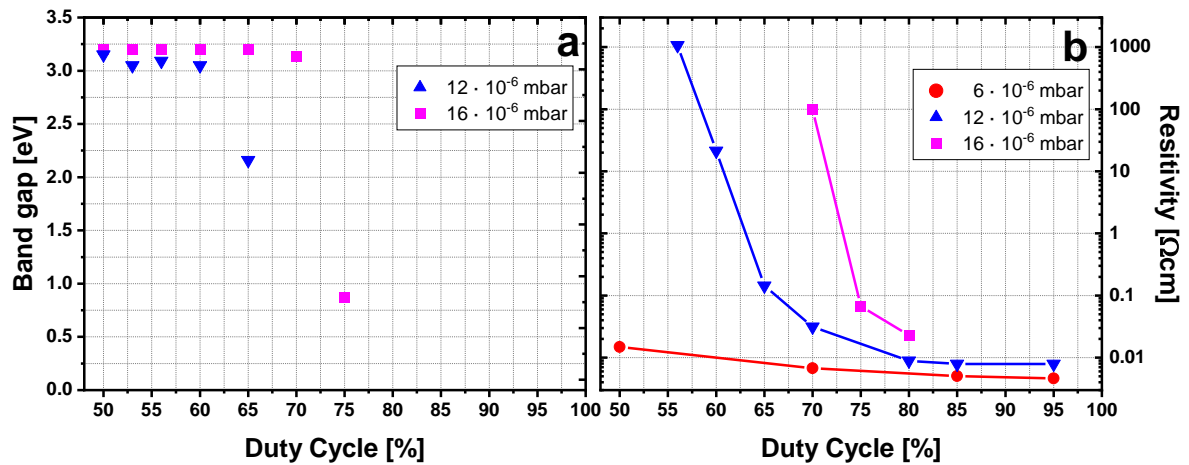
Figure 4-4: Calculated a) band gap and b) resistivity for different oxygen partial pressures at specific duty cycles. The line between the dots is a guide for the eyes

For the samples sputtered at an OPP of $6 \cdot 10^{-6}$ mbar, the bandgap could not be extracted from the Tauc plots since the layers already show metallic behaviour. The samples fabricated at $12 \cdot 10^{-6}$ mbar and $16 \cdot 10^{-6}$ mbar show a band gap E_g between 3.1 eV and 3.2 eV at duty cycles up to 60% and 70%, respectively. This is comparable to literature for the TiO$_2$ band gap [113,144]. No band gap could be extracted from the Tauc plot for a duty cycle higher than 65% and 75% for $12 \cdot 10^{-6}$ mbar and $16 \cdot 10^{-6}$ mbar, respectively. The Tauc plots for the samples fabricated at 65% and 75% duty cycle ($12 \cdot 10^{-6}$ mbar and $16 \cdot 10^{-6}$ mbar, respectively) show a band gap of 2.2 and 0.9 eV. Amorin et al. showed similar results for sputter deposition of titanium oxide [122]. However, the samples in this study show increasing absorption beneath the original band gap of TiO$_2$, as shown below. This can lead to an ambiguous Tauc Plot [145]. A selection of Tauc plots can be seen in the Figure S4-1 in the Supplementary Section.

The influence of the duty cycle on the resistivity of the individual sample is shown in Figure 4-4b. It can clearly be seen that the resistivity decreases with increasing duty cycle for all OPP. Similar to the gdp, the influence on resistivity is higher at higher OPP setpoints and almost disappears at an OPP of $6 \cdot 10^{-6}$ mbar. As noted above, increasing the duty cycle shifts target A to the metallic regime and target B to the oxidic regime. At higher OPP setpoints, this shift begins with a higher duty cycle. Figure 4-4b confirms this trend. Above 80% duty cycle, the resistivity slope flattens and for all OPP the resistivities approaches the value of pure titanium ($7.23 \cdot 10^{-5}$ Ωcm, not shown in the figure), which was deposited at comparable process parameters. However, even at the highest duty cycle, the resistivity of pure titanium is not reached. This can be explained by the high oxygen flow, which still incorporates oxygen atoms into the layer. Figure S4-3 in the supplementary part, which shows the EDX elemental mapping of selected samples, confirms this findings.

As noted above, no band gap could be extracted from the samples prepared at $6 \cdot 10^{-6}$ mbar. Therefore, only OPP of $12 \cdot 10^{-6}$ mbar and $16 \cdot 10^{-6}$ mbar are considered for further investigations. Figure 4-5 shows the influence of the duty cycle on the absorption coefficient for OPP of $12 \cdot 10^{-6}$ mbar and $16 \cdot 10^{-6}$ mbar. From the total absorption coefficient spectra, two wavelengths of interest were selected for further analysis, 300 nm and 500 nm. The total spectra can be found in the Supplementary Section (Figure S4-2). For comparison, the absorption coefficient α of TiO_2 sputtered at 50% duty cycle and 80 sccm oxygen with a thickness of 100 nm is inserted in Figure 4-5 as well.
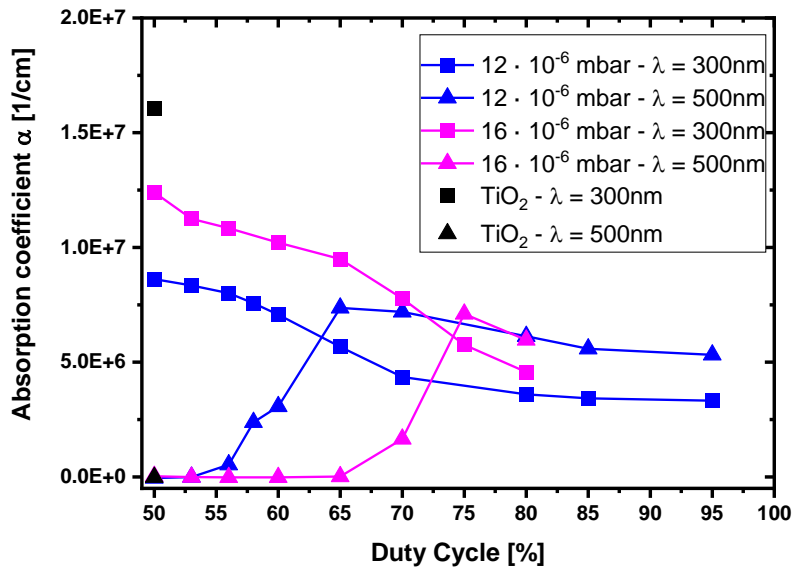

Figure 4-5: Absorption coefficient α at 300 nm and 500 nm for the samples prepared at $12 \cdot 10^{-6}$ mbar and $16 \cdot 10^{-6}$ mbar OPP. For comparison the values of TiO_2 are also inserted

In Figure 4-5, the TiO_2 reference sample shows the highest absorption coefficient at a wavelength of 300 nm. The samples sputtered with lower OPP show a lower overall coefficient. At $\lambda = 300$ nm, a constant decrease can be seen for both OPP when the duty cycle is increased. At $\lambda = 500$ nm, the absorption coefficient is comparable for the three samples prepared at a duty cycle of 50%. Increasing the duty cycle increases the absorption coefficient for both OPPs. This sudden increase occurs at ~56% and ~70% duty cycle, saturates at 65% and at 75% for OPP of $12 \cdot 10^{-6}$ mbar and $16 \cdot 10^{-6}$ mbar, respectively, and leads to a slight decrease for even higher duty cycles. It can be assumed that at this transition the transformation from dielectric-like behaviour to a more metallic-like behaviour takes place. The maximum of the absorption coefficient for each OPP level is in good agreement with the band gap analysis, with the highest absorption coefficient at the last possible band gap extraction. In addition, the change in absorption coefficient is in line with resistivity, confirming the transition into the metallic mode at higher duty cycle. The target with the higher power becomes more dominant and the layers are shifted more into the metallic regime.

4.5 Structural Characteristics

From the previous measurements it can be concluded that at an oxygen partial pressure of $12 \cdot 10^{-6}$ mbar and $16 \cdot 10^{-6}$ mbar the transition from metallic to oxidic regime occurs at 65% and 75% duty cycle, respectively. These two samples and samples near these setpoints were chosen for further investigation. Raman spectroscopy measurements were performed to gain insight into the crystallinity and material composition, see Figure 4-6. The position of the Raman peaks for rutile and anatase titanium dioxide are inserted in the graph for better comparison (as green and blue lines) [146].
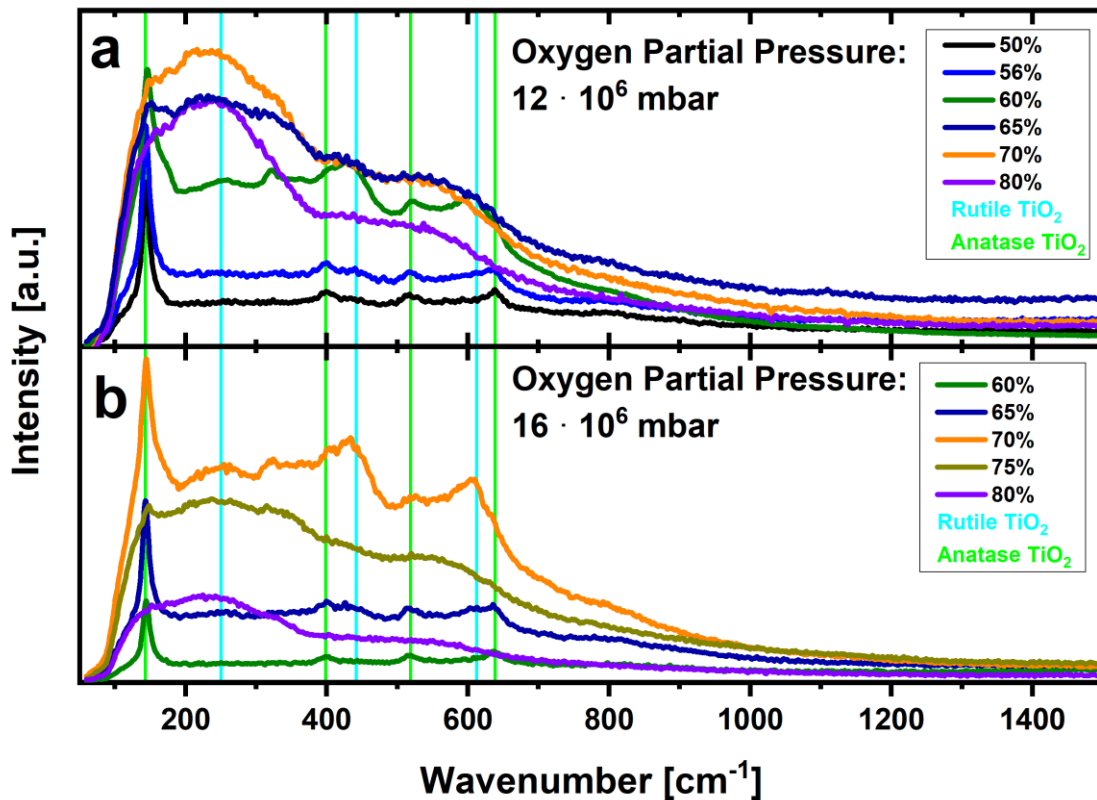
Figure 4-6: Raman signal of selected samples prepared at $12 \cdot 10^{-6}$ mbar and $16 \cdot 10^{-6}$ mbar OPP at specific duty cycles. Insert of theoretical peak positions for rutile (blue line) and anatase (green line) titanium dioxide for better comparison

For both OPPs, the same transformation in the Raman signal can be observed with increasing duty cycles. Close to 50% duty cycle, the signal is very similar to the spectrum of anatase TiO_2. Increasing the duty cycle leads to additional Raman peaks that match the theoretical positions of rutile TiO_2. However, rutile peaks are only visible at 60% duty cycle ($12 \cdot 10^{-6}$ mbar) and 70% duty cycle ($16 \cdot 10^{-6}$ mbar). These spectra also show a peak at ~320 cm^{-1} that cannot be assigned to either an anatase or a rutile phase. However, it has been suggested that such a peak may originate from weak two-photon scattering bands of anatase or a weak rutile or brookite band [147]. Increasing the duty cycle above 60% and

70% at $12 \cdot 10^{-6}$ mbar and $16 \cdot 10^{-6}$ mbar, respectively, broadens the peaks, resulting in one very broad peak around 250 cm^{-1} with a broad shoulder at 500 cm^{-1}. As the Raman spectroscopy analyses the bonds between atoms, slightly different bonds lead to a small shift in the Raman peaks, as in amorphous films. The incorporation of titanium atoms into the layer can disrupt the bond between oxygen and titanium and additionally create defects that lead to slightly different bonds and thus broaden the Raman peak. The higher sputter yield from the high-power target A is the reason for this change of the Raman signal shown in Figure 4-6.

To further study the microstructure, the sample prepared at $16 \cdot 10^{-6}$ mbar OPP and 75% duty cycle was characterized by transmission electron microscopy. Figure 4-7 shows a high-resolution TEM (HRTEM) image of the sample and two area electron diffraction (SAED) patterns taken at two different locations. The system was calibrated through reference samples, both for the TEM and for the SAED measurement. The margin of error lies at approximately 5%.
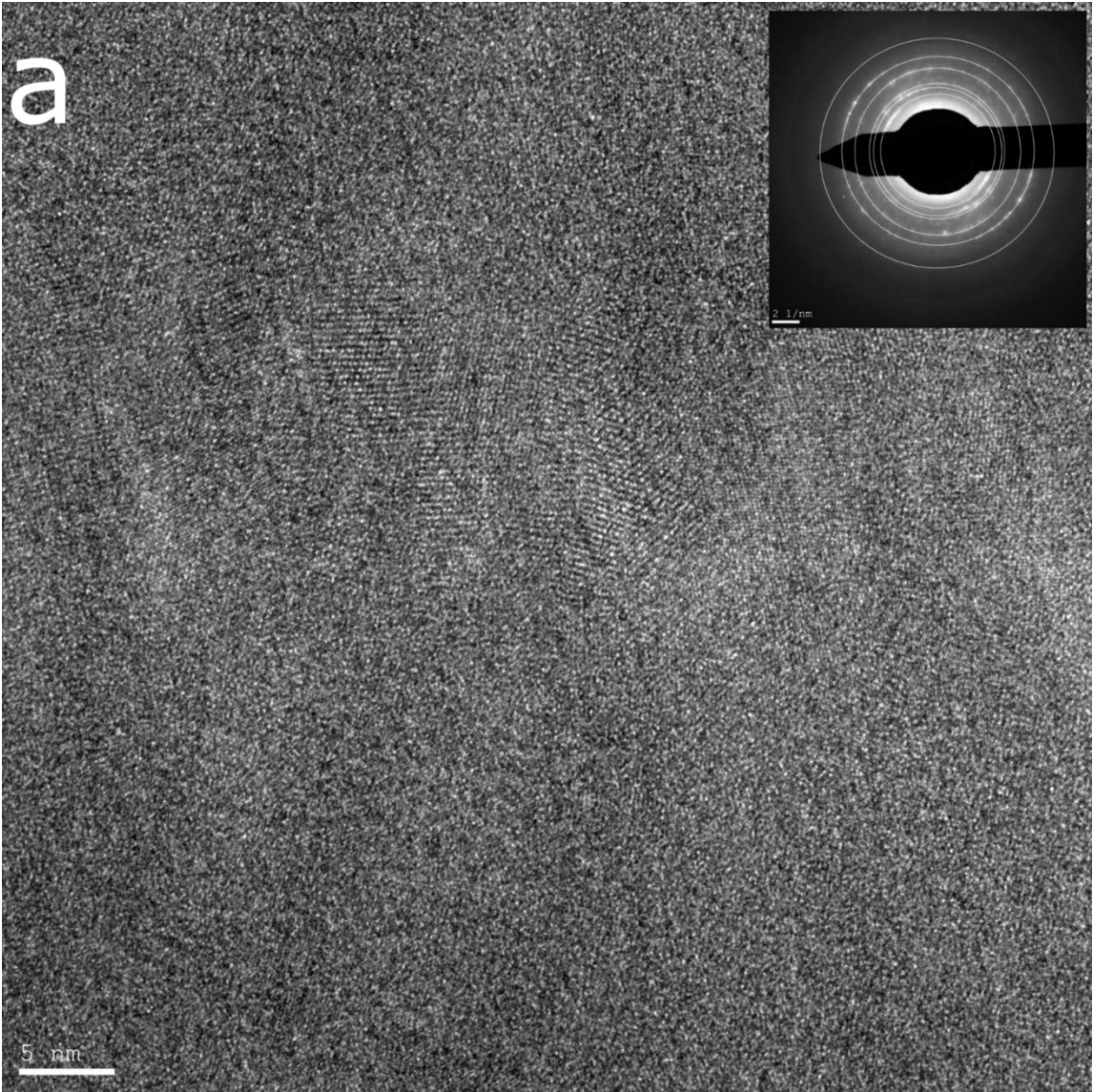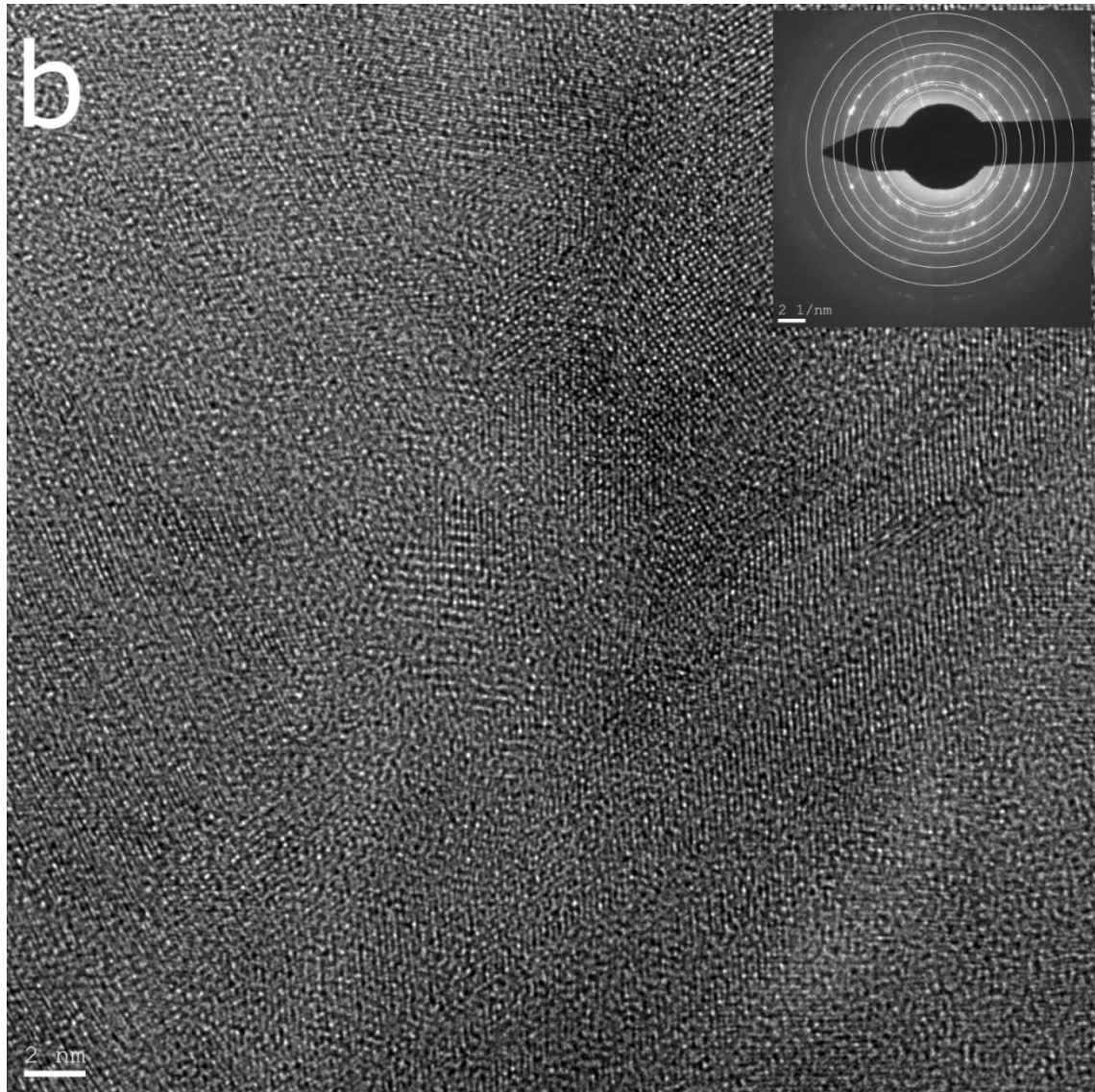
Figure 4-7: HRTEM image of the sample prepared at $16 \cdot 10^{-6}$ mbar OPP and 75% duty cycle at different resolutions, 5nm a) and 2nm b) and inserted two SAED pattern taken at two different spots

The TEM images in Figure 4-7 show that both crystalline and amorphous phases are present in the layer, as concluded by the Raman measurement in Figure 4-6. The corresponding SAED patterns show several reflexes at the same distances. This indicates that the crystals show different orientations of rutile and anatase phases. Furthermore, the blurred parts emphasize the presence of an amorphous phase inside the layer. Table 4-1 provides the theoretical Miller indices of lattice planes of rutile and anatase TiO_2 for each diffraction ring. The best agreements between the theoretical reflex of the crystal structure and the measured radius of the diffraction ring are highlighted. It can be seen that the layers consist of many different crystal orientations of rutile as well as anatase, which is consistent with the Raman measurements in Figure 4-6. The great amount of amorphous structure is in a good agreement with the broad peak of the Raman plot of the same sample in Figure 4-6b.

Table 4-1: Radii of the reflection rings in Figure 4-7 a) and b), left and right, respectively, with the theoretical crystal orientations of rutile and anatase TiO$_2$. The phases that agree best with the measurements are highlighted

g_A [nm^{-1}]	Anatase	Rutile
4.13	(1,0,3)	(1,0,1)
4.63	(1,1,3)	(1,1,1)
4.89	(1,1,3)	(1,2,0)
6.01	(1,2,1)	(2,1,1)
6.88	(2,0,4)	(1,3,0)
8.38	(1,3,0)	(1,2,2)

g_B [nm^{-1}]	Anatase	Rutile
4.18	(0,0,4)	(1,0,1)
4.68	(1,1,3)	(1,1,1)
4.87	(1,1,3)	(1,2,0)
5.98	(1,2,1)	(2,2,0)
6.88	(2,0,4)	(1,3,0)
8.49	(1,3,0)	(1,2,2)
9.75	(2,3,2)	(2,4,0)

4.6 Discussion of the results based on the photoelectrochemical use case

To show the potential of the layers produced by the deposition method, the most promising samples were chosen to analyse their water splitting properties using linear sweep voltammetry (LSV). Only samples that were close to the transformation regime, as discussed in the preceding chapters, were selected for investigation. For the OPP setpoint of $12 \cdot 10^{-6}$ mbar, duty cycles of 53%, 58%, 60% and 65% were included. For the OPP setpoint of $16 \cdot 10^{-6}$ mbar, duty cycles of 70%, 75% and 80% were selected. In addition, a duty cycle of 53% was chosen for the direct comparison between these two OPPs.
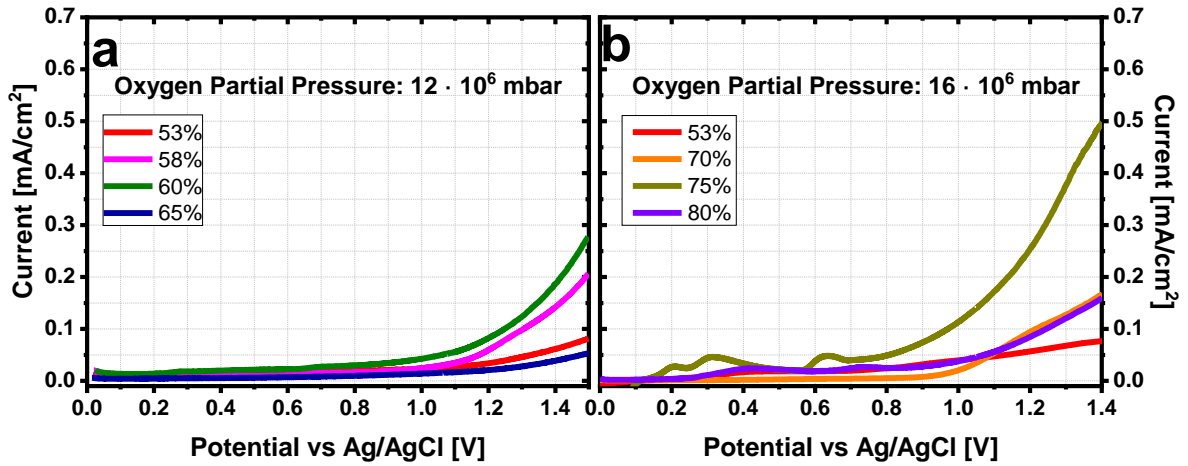
Figure 4-8: Linear sweep voltammetry for selected samples prepared at a) $12 \cdot 10^{-6}$ mbar and b) $16 \cdot 10^{-6}$ mbar at specific duty cycles

Figure 4-8a shows the LSV measurements for an OPP of $12 \cdot 10^{-6}$ mbar. It can be seen that with increasing duty cycle up to 60%, the measured current also increases. Above 60% duty cycle, the current decreases again. For $16 \cdot 10^{-6}$ mbar OPP (Figure 4-8b), the highest current was measured at a duty cycle of 75%. Decreasing or increasing the duty cycle results in a lower current for the LSV measurement, comparable to Figure 4-8a. For the sample sputtered at 75% duty cycle and $16 \cdot 10^{-6}$ mbar, three peaks at 0.2, 0.35 and 0.65 V can be seen in Figure 4-8b. The origin of these peaks is not yet clear. Fabregat-Santiago et al. explained similar findings due to localised states within the band gap [148]. Further investigations on this phenomenon are necessary, but go beyond the scope of this paper.

The comparison of the samples sputtered with a duty cycle of 53% shows comparable current densities for both OPPs. As discussed in Figure 4-6, the Raman measurements of both samples show the typical anatase TiO_2 spectrum. The absorption and the band gap were also comparable, see Figure 4-5 and Figure 4-4a. The oxygen partial pressures are close to each other, as can be seen in Figure 4-3. Therefore, it can be assumed that a sputtering process with a duty cycle of about 50% results in comparable samples for similar OPP. However, increasing the duty cycle leads to a deviation in the properties of the sputtered samples, as shown in the previous chapters.

The highest current of all samples was measured for $16 \cdot 10^{-6}$ mbar OPP at a duty cycle of 75%. This sample shows the highest value of the absorption coefficient at 500nm (see Figure 4-5). Moreover, the sample is located at the transition between metallic and oxidic regime, as shown by the band gap and Raman measurement (see Figure 4-4a and Figure 4-6). For the sample with $12 \cdot 10^{-6}$ mbar OPP and 65% duty cycle, which has similar properties to the just alluded sample, this results in a lower photocurrent, see Figure 4-8a. The oxygen flow and the dynamic deposition rate can be used to explain this discrepancy (see

Figure 4-3b and Figure 4-3c). Compared to the sample produced at $12 \cdot 10^{-6}$ mbar OPP and 65% duty cycle, the oxygen flow during the deposition at $16 \cdot 10^{-6}$ mbar OPP and 75% duty cycle is significantly higher. However, the DDRs for both samples are comparable.

Considering the duty cycle, it shows that target A is closer to the metallic regime than target A in the lower OPP regime. Therefore, due to its higher sputter rate, the main contribution to the thin films comes from this target. As can be seen in Figure 4-3c, increasing the duty cycle while keeping the OPP constant leads to an increase in the DDR. This shows that more titanium is incorporated into the layer at higher duty cycle, which is also confirmed by the EDX elemental mapping shown in Figure S4-3.

The resistivity (see Figure 4-4b) of the sample sputtered at $16 \cdot 10^{-6}$ mbar OPP is lower than the resistivity of the sample sputtered at $12 \cdot 10^{-6}$ mbar OPP, although the oxygen flow is higher. The higher conductivity can be explained by a higher ratio of titanium atoms in the layer, i.e. a layer closer to the metallic regime. For the higher OPP sample the increased current occurred at a higher duty cycle, compared to the lower OPP sample. From the Raman plots in Figure 4-6, clear anatase structures can be seen when both targets are in the same regime (50% duty cycle). At a high duty cycle (e.g. 80%), the Raman plot shows only a broad peak with a broad shoulder, indicating an amorphous layer without a dominant structure. Being in the transition between the metallic and the oxidic regime, like the samples prepared at $16 \cdot 10^{-6}$ mbar OPP and 75% duty cycle, this results in a mixture of an amorphous layer with both rutile and anatase crystal phases. These is confirmed by the TEM characterization in Figure 4-7. From the SAED patterns, it can be concluded that the single crystal structures also differ in orientation, which is in good agreement with the Raman measurement. Yalavarthi et al. has shown that a mixture of rutile and anatase lead to an improvement in photoelectrochemical behaviour [119]. This mixture, together with high absorption and low resistivity, leads to the highest measured photoelectrochemical activity of the characterized samples. Due to the increased absorption, more charge carriers can be created. The low resistivity ensures that many of the charge carriers can flow to the respective contacts. A homogenous distribution of the materials in the layer allows water splitting to take place in the same way on every point of the surface, which increases the resulting photocurrent. Furthermore, the results shown here are comparable to results from other authors, who showed non-doped TiO_2 [107,149–151]. However, a direct comparison with these results is difficult, as there is no standard measurement method [49,104]. Moreover, these samples were micro- and nanostructured, whereas the samples shown here are smooth (see SEM image in Figure S4-3 in the Supplementary Section). It is therefore a reasonable assumption that increasing the surface area of our samples could further increase the photocurrent.

4.7 Conclusion

In this work, we studied the influence of a modified bipolar reactive sputtering process on the optoelectronic, structural and photoelectrochemical properties of TiO_2 thin films. We were able to show that by combining two industrially available sputter deposition techniques, it is possible to increase the absorption and decrease the resistivity of titanium dioxide thin films. This led to a significant increase in the photoelectrochemical water splitting ability. Hereby the samples with the highest inhomogeneity of the crystal structure showed the best photoelectrochemical water splitting ability. Furthermore, the change in the properties of the samples was achieved without additional materials such as hydrogen or other dopants. Only titanium and oxygen were used, thus reducing the complexity of the process, the safety requirements of the deposition device and hence the sputtering tool required. With this hydrogen-free and industry-orientated process we consider the method presented here as an important improvement of the deposition process for an efficient and commercially available titanium dioxide-based photoanode for solar water splitting.

4.8 Acknowledgment

4.9 Funding

5. Publication II: Precise Control of Broadband Light Absorption and Density of Ti³⁺ States in Sputtered Black TiO₂ Thin Films

Dennis Berends, Dereje H. Taffa, Hosni Meddeb, Patrick Schwager, Kai Gehrke, Martin Vehse, Carsten Agert

5.1 Abstract

Defect-rich black titanium dioxide (B-TiO₂) has been extensively studied over the last decade due to its enhanced photoelectrochemical efficiency compared to titanium dioxide (TiO₂), which is known for its outstanding photocatalytic stability. So far, most of the B-TiO₂ material has been obtained by hydrogenation of crystalline TiO₂, resulting in a disordered outer layer of a few nanometers thickness. Recently, a new sputtering process has been introduced to produce B-TiO₂ thin films without the usage of hydrogen. In this work, the influence of the sputtering process on the creation of Ti^{3+} defect states within the films is discussed. Comprehensive optical, structural and electronic studies of the thin film suggest that increasing the density of Ti^{3+} states enhances the conductivity of the films and results in increased and broadband light absorption. In addition, the new sputtering method can also be used to alter the density of the defect states in the film in a controlled manner, allowing the optical and electronical properties of the thin film to be changed in a precise and controllable way.

5.2 Introduction

Thin films of titanium dioxide (TiO₂) are attractive for various modern applications, of which photocatalytic processes are among one of them. The thin films can be prepared in many different ways, e.g., reactive sputtering, ultrasonic spray pyrolysis, sol-gel process, electrochemical deposition processes or pulsed laser deposition [110,111,116,152]. The number of possible photocatalytic processes is at least as large as the number of possible deposition methods. TiO₂ has been widely used for reduction of carbon dioxide (preventing or reducing the climate change), water purification (increasing the amount of drinkable water) and water splitting for hydrogen production (long-term storage of energy) [18,114,153–156]. However, due to its wide band gap of 3.3 eV, using stochiometric TiO₂ for these processes results in low photocatalytic efficiencies. By increasing the spectral absorptivity of the material, the efficiency of the respective photoelectrochemical process can be increased.

Generally, this is done by reducing the band gap, either by doping with additional elements like carbon, vanadium, iron or by self-doping, where defect states within the band gap are introduced [65]. Depending on the type of deposition methods and the amount of defect states present, the optical absorption and thus the color of TiO_2 changes. When the density of defects is high enough, the layer turns black and shows a broad band absorption [121]. In 2011, Chen *et al.* were the first to report a synthetic approach to prepare defect-rich black TiO_2 (B-TiO_2). Through hydrogenation of TiO_2 nanoparticles in a high-pressure hydrogen atmosphere, the outer layer became disordered and turned black resulting in a so-called core-shell particle. Since then, the interest in B-TiO_2 has increased and several different methods for the preparation of black TiO_2 have been published [17,19,64,120,157]. One of the most common methods to create these defects is the controlled treatment of TiO_2 in a reducing atmosphere, e.g., a hydrogen plasma or annealing in hydrogen gas [158–160]. Only a few reports have demonstrated the creation of defect rich B-TiO_2 without the use of hydrogen, for example by reactive sputtering of sub stoichiometric TiO_x layers [155,161]. Moreover, several applications have been identified where B-TiO_2 shows an increased efficiency compared to TiO_2, e.g., photoelectrochemical water splitting, carbon dioxide reduction, water purifications, or cancer treatment [11,18,64,77]. In black TiO_2 free charge carriers occur mainly through Ti^{3+} states. These states are considered to influence the catalytic behavior of the material during photoelectrochemical reactions. Thereby, an increase in the Ti^{3+} states correlates with an increase in reactivity and efficiency [162,163]. Controlling the amount of these states is therefore of great interest. To our knowledge there are no other reports that show precise control of the Ti^{3+} density via a single process parameter during the deposition.

In this study, we demonstrate a bipolar reactive sputtering method of B-TiO_2 and show that the absorption and the amount of Ti^{3+} states can be precisely adjusted. The process does not require hydrogen and only one sputtering parameter is changed. The sputtering process is driven within an oxygen hysteresis, resulting in sub stoichiometric thin films. The samples are characterized by UV-Vis spectrophotometry, X-ray photoelectron spectroscopy (XPS) and X-ray diffraction (XRD) measurements. To investigate the band structure of the samples the O'Leary-Johnson-Lim (OJL) and the extended Drude model are fitted to the measured transmission and reflection data [164]. The results show that the increase of the free charge carrier occurs through the formation of defect states within the band gap, leading to a new valence band maximum and an increased penetration of the band tails into the band gap.

5.3 Results & Discussion

As described in more detail in the methods and experimental section, the power distribution (duty cycle, DC) between the two metallic titanium targets was gradually increased, from 71% to 83%. The optical absorption spectra (A=1-T-R) as well as the measured transmission and reflection spectra of the samples prepared with increasing DC are shown in Figure 5-1.
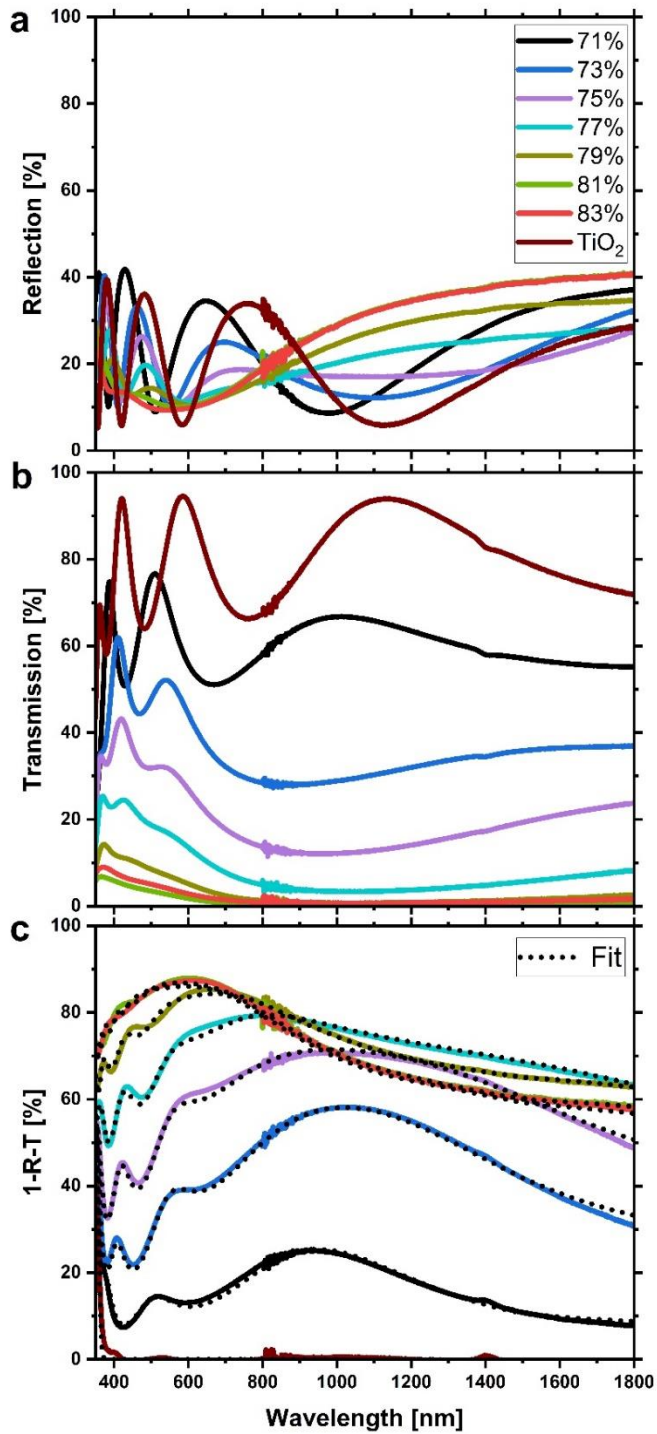
Figure 5-1: a) Reflection and b) Transmission curves of the samples; c) Absorption (1-R-T) measurement and corresponding fits of the respective samples. For better illustration, only every second DC is displayed. The black dots represent the fitted curves of the corresponding measured values (solid line).

It can be seen that the transmission decreases steadily with increasing DC (Figure 5-1b). The reflection (Figure 5-1a), on contrast, shows two regimes. At lower wavelengths (up to 800 nm), the reflection decreases as well. Above 800 nm, however, the reflection increases again. The following experiments indicate that the layer properties change from an isolator-like into a metallic-like material with increasing DC, although neither a pure isolator or metal layer is produced by this inhomogeneous process. This was also confirmed by our previous study [155]. From Figure 5-1c it can be seen that the broadband absorption becomes more pronounced with increasing DC. The peaks around 450 nm can thereby directly be related towards defect states inside the thin film [165]. However, for the sample sputtered at 79% DC, the absorption starts to slightly decrease again for wavelength $\lambda > 800$ nm. Here, the increased reflection due to the metallic behavior of the layer gets more dominant, which also explains the broadening of the peak around 450 nm. For DC > 81% no change in the optical properties can be observed. This can be seen as the curves for the 81% and 83% DC samples overlap. In addition, it can be seen in Figure 5-1 that the pure TiO_2 sample absorbs only at wavelengths below 380 nm.

The band gap of the pristine TiO_2 sample, as calculated by the OJL model is $E_g = 3.51 \pm 0.02$ eV. This is in good agreement with literature [166,167]. The band gap values of the samples sputtered within the low oxygen regime remain almost the same $(3.54 \pm 0.03$ eV). It can be concluded that the band edges (without defect tail states) remain fixed and the increased absorption may have another reason. To gain further insight into the structure of the samples, we studied their crystal phases. The XRD measurements of the samples along with images of the respective samples are shown in Figure 5-2.
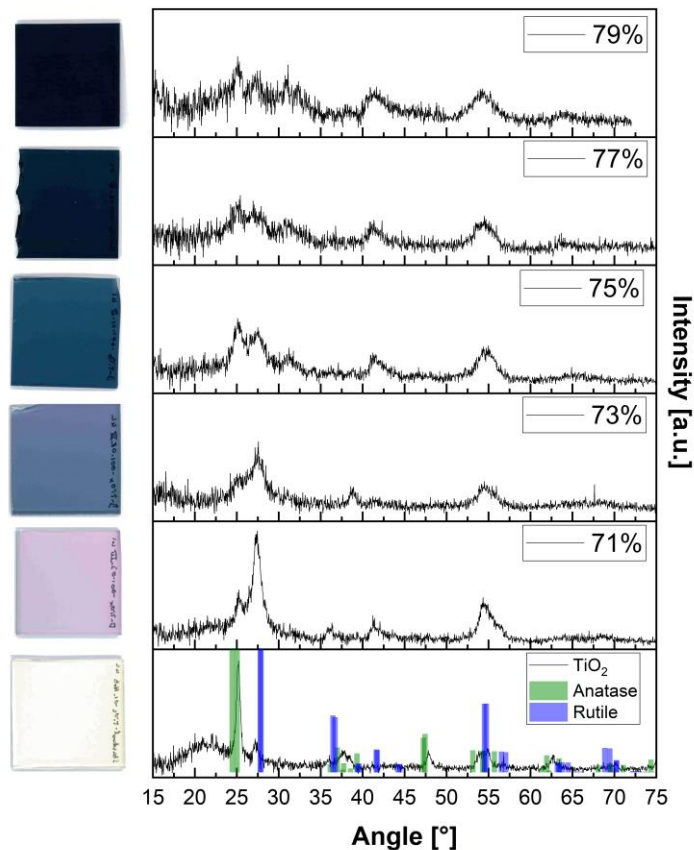
Figure 5-2: Left: Images of the samples corresponding to the XRD measurement. Right: XRD measurements of the samples. In the bottom row theoretical values for anatase (ICDD reference code: 00-021-1272) and rutile (ICDD reference code: 00-016-0934) peaks are shown.

Figure 5-2 shows that the color of the B-TiO$_2$ changes as the DC increases. While the TiO$_2$ sample (Figure 5-2 bottom row) is transparent, the non-stoichiometric sample sputtered at 71% DC has a purple color. With increasing DC, the color changes from blue to black. The XRD measurements for the TiO$_2$ sample indicate a dominant anatase crystal structure (Figure 5-2 highlighted in green). Being within the oxygen hysteresis, the sample sputtered at 71% DC exhibits a mixture of anatase and rutile structures as indicated by the XRD measurement. However, the intensity of the rutile phase increases drastically at 71% DC compared to the TiO$_2$ sample and decreases again until 75% DC. This behavior can be explained by the increased amount if titanium inside the layer, as shown in our previous publication [155]. Through this additional implementation, the thin films become more dense which promotes rutile phases above anatase phases [168]. Increasing the DC further broadens the main peaks. At 77% DC only some small rutile peaks with no anatase structures can be seen. The samples do not exhibit a dominant crystal structure and seem to be amorphous [169]. The further increase of titanium atoms in the layer disturbs the formation of crystal structures.

To get more insight into the morphology of the samples, SEM measurements were done. For selected samples these images are shown in Figure 5-3.
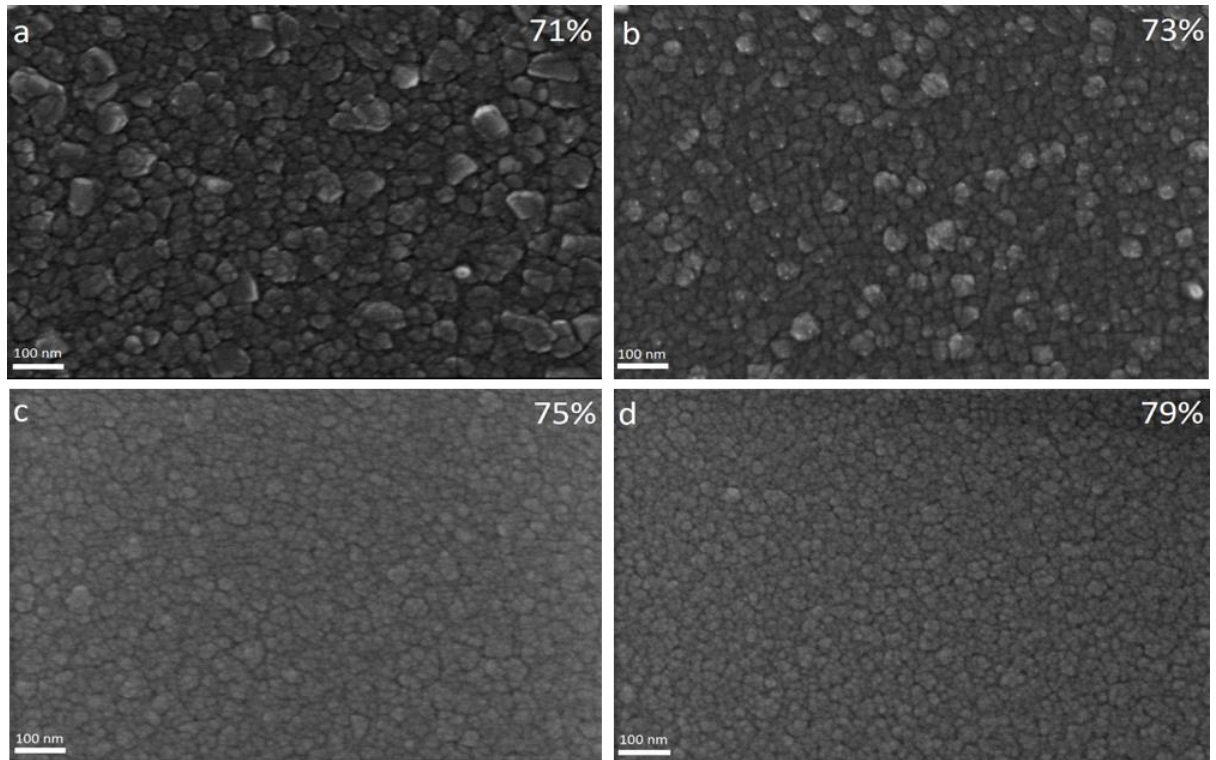
Figure 5-3: SEM images of the sputtered samples, taken at 100k magnification. a) 71% DC; b) 73% DC; c): 75% DC; d) 79% DC.

From the SEM images in Figure 5-3 can be concluded that the samples consist of grains in the sub-micrometer range. With increasing DC the size of the grains decreases, which is supported by the decreasing intensity of the XRD peaks as shown in Figure 5-2.

To understand the increasing of absorption shown in Figure 5-1, the plasma frequency for each sample has been calculated using the Drude-Lorentz model. In addition, XPS measurements were performed and the ratio of the peak area of Ti^{3+} to Ti^{4+} states was calculated. The Ti^{3+} states can be associated with defects formed inside the band gap [170]. Furthermore, the dark conductivity of the samples was measured. The results are presented in Figure 5-4.

Figure 5-4: a) XPS measurements of the Ti 2p spectra; b) fitting of the Ti^{3+} and Ti^{4+} states to the corresponding peaks, exemplarily shown for the sample sputtered at 75% DC; c) Ratio of the Ti^{3+} and Ti^{4+} states of the investigated samples, derived from the fitted peak area (inserted table) of the XPS measurements (black) and the plasma frequency of the samples calculated through the Drude-Lorentz model with error given by the software (red); d) Dark conductivity of all samples.

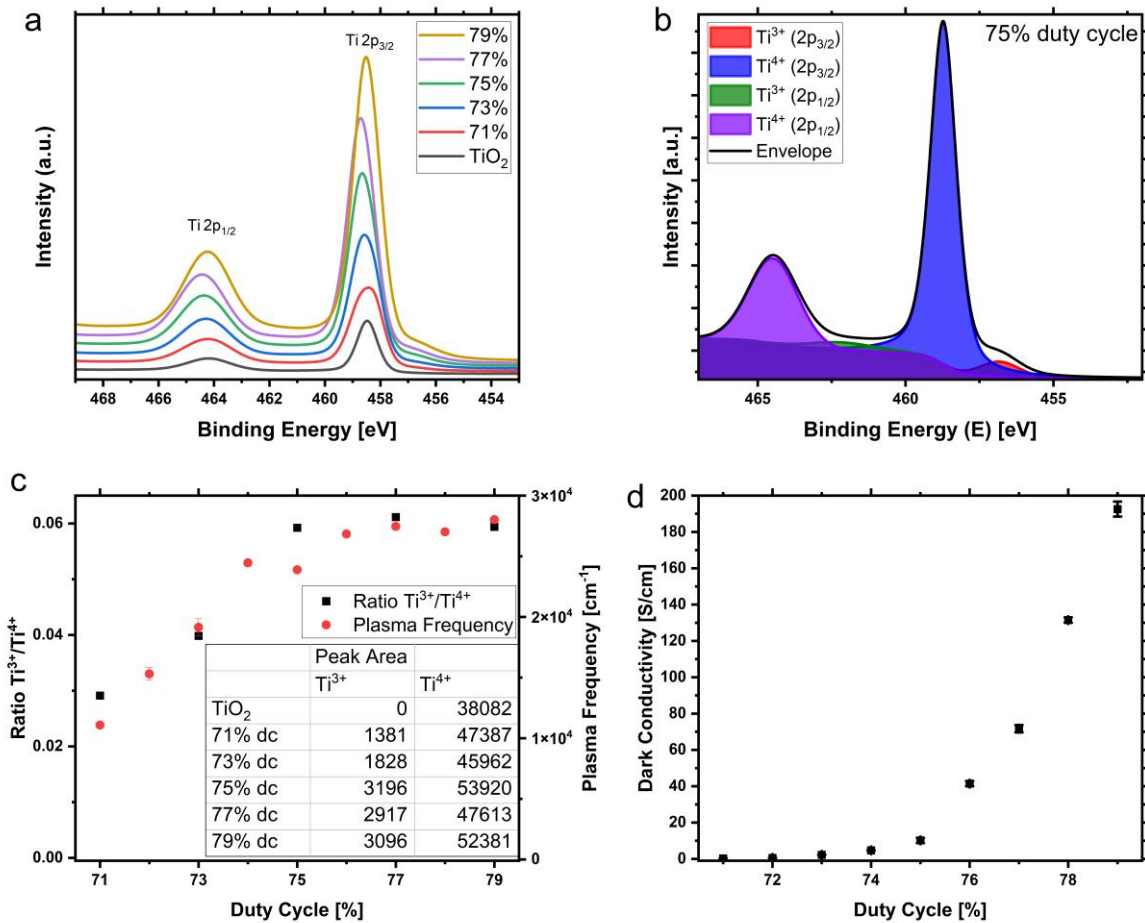The Ti 2p XPS envelope spectra of the samples are shown in Figure 5-4a. For each peak, the Ti^{3+} and Ti^{4+} states were fitted, exemplarily shown in Figure 5-4b. No Ti^{3+} states were detected for the TiO_2 sample, which correlates with the absence of defects, and therefore no plasma frequency could be calculated [171]. With increasing DC, the Ti^{3+} peak centered at 457 eV increases. The ratio of the peak areas of the Ti^{3+} states to the Ti^{4+} states confirms this trend (Figure 5-4c). At 75% DC the ratio converges. However, as the DC increases, the plasma frequency increases until 76% DC, where it reaches saturation, supporting the trend as seen for the amount of free charge carriers. However, the dark conductivity in Figure 5-4d shows an exponential increase whereas the crystal size decreases (as shown in Figure 5-3) for increasing DCs, as shown in Figure 5-3. To understand this phenomenon of increasing absorption shown in Figure 5-1, especially for samples with a DC of more than 75%, the OJL model must be studied in more detail. Since the number of defect states

does not continue to increase with higher DC, as shown in Figure 5-4c, the damping constant calculated with the gamma function γ must be considered first. The gamma function of the OJL model is helpful to describe the tail states that enter the band gap. A decreasing value reflects a decreasing distance between the band tails [172]. The value of this function is shown in Figure 5-5.
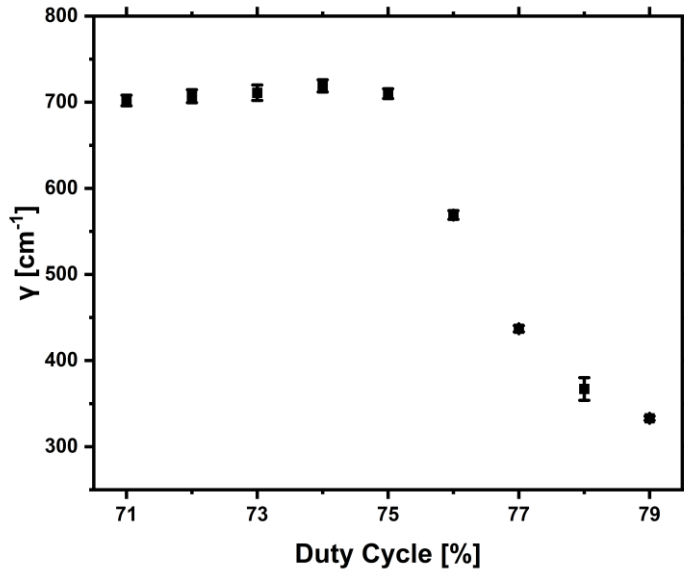
Figure 5-5: Gamma function, derived from the OJL model.

The plot of the the gamma function from the OJL model shows that the samples between 71% and 75% DC have an increased amount of band tail states compared to the TiO_2 sample (1025 cm^{-1}, not shown). These samples were sputtered within the oxygen hysteresis and are therefore defect rich as expected [173]. A further decreasing gamma function for samples above 75% DC can also be seen. As the DC increases, the band tail states penetrate deeper into the band gap even though the number of defects is saturated. For samples sputtered with a DC of more than 79%, the gamma function value saturates (not shown). Different kind of defect states inside the band gap can be the reason for the increased tail states and thus provide the explanation for the increased absorption and dark conductivity of the samples. In another study, the influence of the different degrees of localization were investigated [174]. Di Valentin et al. claim that different defect states are created within the band gap depending in the localization. While the amount of Ti^{3+} states remains, their localization can change, giving the explanation for the increased band tail states. However, the band gap derived by the OJL model does not consider these tail states. Therefore, the valence band maximum (VBM) was determined by XPS measurements and can be related to the conduction band minimum (CBM). Figure 5-6 shows the VBM, the activation energy and the calculated band gap of the OJL model in relation to the CBM (set at 0 eV).

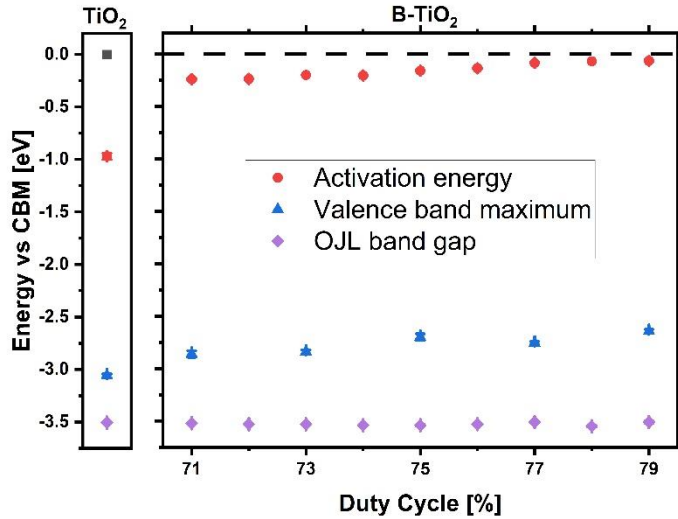Figure 5-6: Valence band maximum, activation energy, and band gap (derived by the OJL model) of the samples relative to the conduction band minimum (set to 0 eV).

It should be noted that the VBM refers to the Fermi level of the corresponding sample [175]. Therefore, dark conductivity measurements were performed to calculate the activation energy. It indicates the Fermi level relative to the conduction band. The activation energy of our TiO_2 sample is in good agreement with reported literature [176]. In addition, a clear decrease in the activation energy from 0.97 eV for the TiO_2 sample towards 0.24 eV for the sample sputtered at 71% DC can be observed. With further increase of the DC a decrease in the activation energy can be seen. Above 77% DC the values tend to saturate.

For the TiO_2 sample, the band gap energies given by the difference of CBM and VBM and by the OJL model show a small off set. The OJL model calculates the band gap without the presence of the band tails. However, band tails were calculated for this sample by the Drude model. Therefore, the band gap derived from the VBM measurement is lower than what was calculated with the OJL model, as the band tails are considered at the former method. The difference between CBM and VBM slightly decreases for the samples prepared at different DCs and at $16 \cdot 10^{-6}$ mbar oxygen partial pressure, although it is significantly smaller than the VBM for the TiO_2 sample. Tan *et al.* reported a change in the crystalline structure from anatase to rutile phase with the VBM rising of about 1.0 - 1.5 eV [177]. The crystal structure of the samples shown here exhibit a similar change as indicated by the XRD measurements in Figure 5-2.

5.4 Conclusion

A systematic analysis of the structural, optical and electrical properties of black TiO_2 samples prepared by a modified bipolar reactive magnetron sputtering technique was performed. It was demonstrated that the absorption of B-TiO_2 can be precisely changed by varying only the power distribution between the two titanium targets. These findings provide further insights into the properties of sputtered black TiO_2 thin films without hydrogen treatment and without a core-shell structure. Fitting of the optical data with different models suggest that the density of the Ti^{3+} states can be modified in a controlled manner up to a certain duty cycle. Above this duty cycle, the width of the tail states within the band gap increases, explaining the increased absorption and enhanced dark conductivity. Furthermore, the reduced band gap can help to fabricate a material suitable for various applications, e.g., tandem photoelectrochemical cells. In addition, the catalytic efficiency of many different reactions can be improved through the controlled implementation of the Ti^{3+} states. It can also be assumed that, on the one hand, a change of the oxygen partial pressure shifts the position of the duty cycle at which the maximum of Ti^{3+} states are reached. On the other hand, a lower oxygen partial pressure can lead to a further decreased band gap and thus increase the variability of the black TiO_2.

5.5 Methods and Experimental section

5.5.1 Sample preparation

The samples were prepared by closed-loop reactive bipolar magnetron sputtering using the in-line vacuum system Vistaris 600 (Singulus Technologies AG, Germany). Two cylindrical titanium targets (purity 3N) with a length of 600 mm and a diameter of 155 mm were used. The total power of 8 kW is distributed between the two targets from 71% towards 83% DC to deposit samples (10 x 10 cm) with varying defect density. Through closed feedback control the oxygen flow was kept inside the oxygen hysteresis, resulting in a constant oxygen partial pressure and in non-stoichiometric films. A detailed description of the process can be found in Berends et al. [155]. The produced layer thicknesses are in the range of 240 – 270 nm. For the electrical measurements two 1 x1 cm^2 silver contacts were deposited on top of the via electron beam evaporation (VTD Vakuumtechnik Dresden GmbH, Germany). An area of 0.1 x 1 cm was left uncoated in the middle of the two silver contacts.

5.5.2 Characterization methods

Transmission (*T*) and reflection (*R*) measurements were carried out in a Cary 5000 UV-Vis-NIR spectrophotometer using an integrating sphere (Agilent Technologies Inc., USA) in the wavelength range from 300 to 2000 nm. The thickness (*d*) of the deposited films was measured using a Dektak 150 stylus profilometer (Veeco, USA). The thin film optics software CODE/Scout (WTheiss Hardware and Software, USA), which uses the 1D transfer matrix method, was used to create optical models of the samples, using transmission and reflection measurements. The OJL model as well as the Drude-Lorentz model were chosen in the software. The OJL model describes the band gap transition by using the band gap energy $E_{g,\,OJL}$ as well as a parameter to account for the exponential tail γ penetrating into the band gap [164]. The Drude-Lorentz model allows for calculating the plasma frequency ω_p using the free-electron density n_e, e.g. $\omega_p = \sqrt{n_e e^2 / m_e \varepsilon_0}$. This parameter represents the density of defect states in the thin film. The remaining parameters describe the electron charge e, the material related effective electron mass m_e and the vacuum permittivity ε_0 [178].

Chemical state (oxidation state) analysis was performed through X-ray photoelectron spectroscopy (XPS) measurements in an ultra-high vacuum set-up. The ESCALAB 250 Xi (Thermo-Fisher, UK) equipped with a monochromatic Al Kα X-ray source (hv = 1486.6 eV). High-resolution spectra were recorded for the C 1s, O 1s, N 1s and Ti 2p photoelectron lines. A pass energy of 10 eV and a step size of 0.02 eV was chosen. Valence band XPS spectra were measured at a pass energy of 20 eV with an energy resolution of 0.05 eV. The binding energy scales were calibrated to the most intense C 1s peak at 284.8 eV. The Avantage software (version 5.9925, Thermo Fisher Scientific, USA) was used to analyze the spectra.

Dark conductivity (σ_d) measurements were performed using the two-point probe technique. A constant bias voltage of 5 V was applied, and the current was measured using a Keithley 2636A (Keithley Instruments, USA). The samples were heated in vacuum up to a temperature T of 120°C and then passively cooled to 50°C. The temperature was measured with a Pt100 probe. According to the Petritz model, the dark conductivity can be calculated using the relation $\sigma_d = \sigma_0 \exp(-E_a k^{-1} T^{-1})$, where σ_0 is a constant, k the Boltzmann constant and E_a the activation energy [179]. The activation energy is contributed to localized states close to the Fermi level [180].

To get insights of the crystal structures and phase composition of the samples grazing incident x-ray diffractograms (XRD) measurements were performed with a PANalaytical Empyrean diffractometer (Malvern PANalytical, Netherlands) with CuKα = 1.54 Å

radiation at an incident angle of 0.2°. The diffractograms were recorded over a range of $2\Theta = 15–80°$.

To create images of the sample a Zeiss Neon 40 EsB crossbeam scanning electron microscope (Carl Zeiss Ag, Germany) was used.

5.6 Acknowledgment

5.7 Conflict of Interest

The authors declare no conflicts of interest.

6. Publication III: Analysis of the Inhomogeneous Growth of Sputtered Black TiO$_2$ Thin Film

Dennis Berends, Patrick Schwager, Kai Gehrke, Martin Vehse, Carsten Agert

6.1 Abstract

Black titanium dioxide (B-TiO$_2$) is a highly active photoelectrochemical material compared to pure titanium dioxide due to its increased light absorption properties. Recently, we presented the deposition of thin film B-TiO$_2$ using an asymmetric bipolar reactive magnetron sputter process. The resulting samples exhibit excellent photoelectrochemical properties, that can be fine-tuned by varying the process parameters. In this article, results of morphological, electrical and photoelectrochemical measurements are discussed to better understand the surprisingly high electrochemical activity of the films. In order to study the influence of the dynamic process on the film formation, we use static sputtering with a fixed substrate covering the entire chamber area in front of the two targets. This allows the material composition of the sputtered film to be analyzed depending on its relative position to the targets. The results lead to the conclusion that the asymmetric bipolar sputtering mainly produces two phases, a transparent, non-conductive crystalline phase and a black, conductive amorphous phase. As a consequence, the dynamically sputtered samples are multilayers of these two materials. We discuss, that the significantly better electrical and photoelectrochemical properties emerges from the inhomogeneous nature of the laminates, like it is also found in core shell nanoparticles of B-TiO$_2$.

6.2 Introduction

Black titanium dioxide (B-TiO$_2$) has proven to be a highly efficient material, especially in the field of carbon dioxide reduction and photoelectrochemical water splitting for green hydrogen production. [19,62,68,69] Over the past decade, the interest in B-TiO$_2$ has steadily increased in the photocatalytic community.[18,64,181,182] To date, most of the B-TiO$_2$ materials are prepared by hydrogen treatment of anatase TiO$_2$ nanoparticles.[160,183] The resulting core-shell particles possess a nonstoichiometric amorphous outer shell and are highly light absorbing.[20] Especially with regard to thin film sputtering, publications showing an alternative process for the deposition of B-TiO$_2$ are rare. Escaliante et al. prepared a multilayer TiO$_2$/TiO$_{2-x}$/TiO$_2$ film.[161] During the reactive sputtering of TiO$_2$, they periodically stopped the oxygen flow to create the sub-stoichiometric TiO$_{2-x}$ layers. They show that

their samples exhibit an enhanced photocatalytic response compared to pristine TiO_2. Another way to produce a $B-TiO_2$ thin film is by sputtering pristine TiO_2 thin films and post-treat the samples after deposition using a hydrogen plasma. [184] Samples prepared this way are highly absorptive in the UV-visible range and show a good conductivity. By introducing hydrogen directly into the plasma during the sputter process a uniform $B-TiO_2$ can be formed.[185,186] This leads to an enhanced photoelectrochemical activity compared to pristine TiO_2, as the optical absorption is increased. Recently, we have presented a new hydrogen-free bipolar sputter process for the deposition of $B-TiO_2$ thin films.[155,187] This asymmetric dynamic nature of the process results in layered films, that show a very high photoelectrochemical activity when compared to pristine TiO_2. The inhomogeneous films sputtered this way exhibit alternating crystalline and amorphous phases. Similar structures can be found in core-shell $B-TiO_2$ nanoparticles. The physical background as to why this structure is beneficial has already been investigated in detail.[63,66,188] However, such investigations are lacking for thin-film $B-TiO_2$. Due to the similarity in the structure, similar reasons for the increased photoelectrochemical activity can be assumed. This investigation is the subject of this article.

In order to investigate the underlying reason for the enhanced photoelectrochemical properties of the $B-TiO_2$ thin films, the microstructure and properties of the dynamic sputtered $B-TiO_2$ thin films are studied in detail. We show how the individual sputter phases of this asymmetric process contribute to the improved properties of the thin film. For this, the dynamic part of the process is transformed into static sputtering, i.e. the substrate is kept at a fixed position in front of the targets instead of being moved. This transformation makes it possible to analyze the different forming phases and investigate their properties. The individual phases are characterized in terms of their electrical, morphological and photoelectrochemical properties. The results are used to discuss how an alternating structure of the crystalline and amorphous phases leads to an enhanced photoelectrochemical water splitting ability of the dynamic sample, comparable to the core-shell structure of $B-TiO_2$ nanoparticles.

6.3 Methods

Sample preparation: Samples were prepared by closed-loop reactive bipolar magnetron sputtering using the Vistaris 600 inline vacuum system (Singulus Technologies AG, Germany). Two cylindrical titanium targets (purity 3 N) with a length of 600 mm and a diameter of 165 mm were utilized. The total power of 8 kW was distributed 75% to the left target and 25% to the right target. As substrates 10x10 cm and 30x30 cm soda-lime glass

was taken. A closed-loop feedback control was applied to keep the oxygen flow at a constant oxygen partial pressure. The substrate temperature was set to 200 °C. In the dynamic process, the carrier on which the substrate is mounted passes the targets several times. Sample from this process type will be referred to as "dynamic samples" in the course of this article. During the static process, two 30x30 cm glass substrates, mounted on the carrier, were placed stationary in front of the targets inside the sputtering chamber by omitting the carrier movement during deposition. Sample from this process type will be referred to as "static samples" in the course of this article. The sputtering chamber is 58 cm long and therefore the substrates can cover the entire chamber. The sputtering time was set to 15 minutes. A detailed description of the dynamic process can be found in an earlier study.[155]

Characterization Methods: The thickness d of the produced samples was measured by a Dektak 150 stylus profilometer (Veeco, USA). The sheet resistance $R_\square$ was measured with a Jandel RM3-AR four-point probe station (Jandel Enigneering LTD, UK). The measured sheet resistance and thickness were used to calculate the resistivity $\rho = R_\square \cdot d$. To analyze the crystal structure, Raman measurements were performed using a Senterra system with a 488 nm laser (Bruker Corporation, USA). High-angle annular dark-field imaging in a scanning transmission electron microscope (HAADF-STEM) and energy-dispersive X-ray spectroscopy (EDX) line scans measurements were performed by a FEI Titan 80/300 G1 transmission electron microscope (Field Electron and Ion Company, USA). Electrochemical characterization of the materials was performed by a VersaSTAT 4 potentiostat (Ametek Scientific Instruments, USA). Linear sweep voltammetry (LSV) was done in a three-electrode setup with an Ag/AgCl reference electrode and a platinum wire as a counter electrode (surface area of 83.68 cm^2). The deposited B-TiO$_2$ layers served as the working electrode with an active area of 0.785 cm^2. A 1 M KOH solution (pH = 13) was taken as the electrolyte. The scan rate of the LSV measurement was 10 mV/s. A solar simulator with AM 1.5G (1000 W/m^2) was used for visible light irradiation.

6.4 Results and Discussion

Due to the moving substrate the dynamic asymmetric sputter process, by nature leads to an inhomogeneous growth of the B-TiO$_2$ thin films. In the vacuum chamber, the glass substrate first moves along the left target and then the right target, see Figure 6-1. After passing both targets, the direction of the substrate changes and it moves from right to left. This process was repeated seven times.
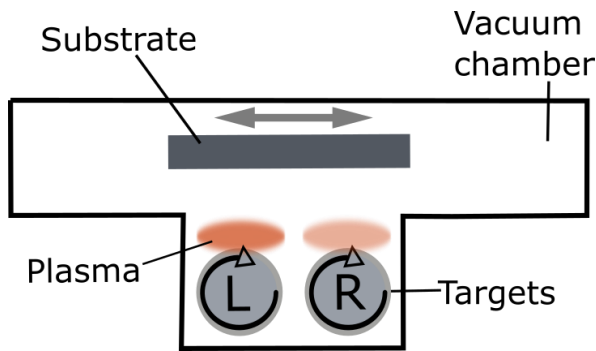
Figure 6-1: Schematic Drawing of the sputter chamber. Inside the vacuum chamber the substrate moves in front of the two rotary targets, left (L) and right (R). To emphasize the higher power of the left target, the plasma is colored darker.

An EDX line scan was performed to measure the distribution of titanium and oxygen atoms in the dynamic sample and can be seen in Figure 6-2. A HAADF-STEM image of a cross-section of the thin film is also shown.
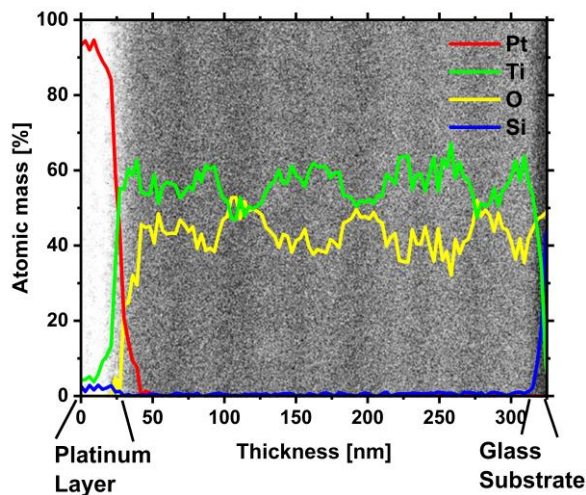
Figure 6-2: HAADF-STEM image and EDX line scan of a cross-section of the sputtered B-TiO$_2$ thin film. The platinum protection layer and the glass substrate can be seen on the left and right edges, respectively. The growth direction of the layer is from right to left.

The EDX measurement in Figure 6-2 shows the titanium (Ti) and oxygen (O) as well as the platinum (Pt) and silicon (Si) distribution in the cross-section of the dynamic sample. It can clearly be seen that there are alternating areas of higher oxygen and lower titanium content. In addition, the line scan shows the glass substrate on the right and the protective platinum layer on the left side. The alternating areas can also be distinguished through the different contrast areas in the HAADF-STEM image. This structure can be explained by two different aspects of the process. First, by the dynamic character of the sputter process and second, by the asymmetric power distribution of the targets. The latter has the effect that the oxidation state, i.e. the composition of the sputtered material, differs between the

left and the right target. Since the sample moves back and forth seven times in front of the targets, an alternating structure can be expected. This is confirmed by the EDX data and the STEM image. Further details about the process can be found elsewhere.[155]

In order to gain a deeper understanding of the B-TiO$_2$ thin film growth, static sputtering experiments were performed, i.e. the glass substrates were placed in front of the targets and the movement of the carrier was omitted. In this way it is possible to record the local growth conditions at each position in the chamber. Figure 6-3 shows a section of the overall static sample. In addition, the positions of the two targets in relation to the static sample are depicted schematically. For a better visualization, an image section of the static samples is shown.
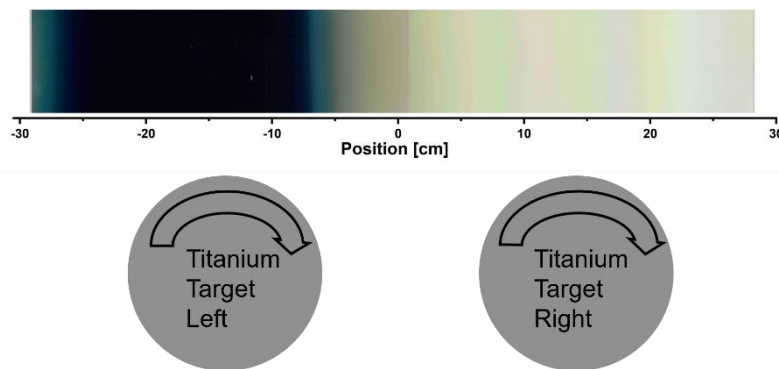
Figure 6-3: Stationary growth: Two glass substrates are fixed in front of two rotating targets. The dimensions and positions of the targets correspond to the position of the sample.

The lateral positions of the centers of rotation of the two titanium targets are at -13 cm and +13 cm in front of the sample, respectively. The targets were operated at different powers, 6 kW on the left and 2 kW on the right. Furthermore, Figure 6-3 shows that a black layer growths in front of the left target, while the layer that grows in front of the right target appears transparent.

To get more information about the growth process, the thickness of the static sample was measured at different positions. In addition, a Gaussian fit was performed on the two peaks of the deposition rate. With this, the growth of the dynamic sample for seven layers can be calculated.

Figure 6-4: Layer growth analysis of the static and the dynamic sample. a) Measured thickness and corresponding deposition rate of the static sample for different positions. A gaussian peak fit is included for each of the two targets. For a better visualization of the position, an image of the sample is shown above the graph. b) From the fits the layer thickness growths of the dynamic sample over time was calculated. For a better visualization the fitted deposition rates of both targets are shown as well. In the background the HAAD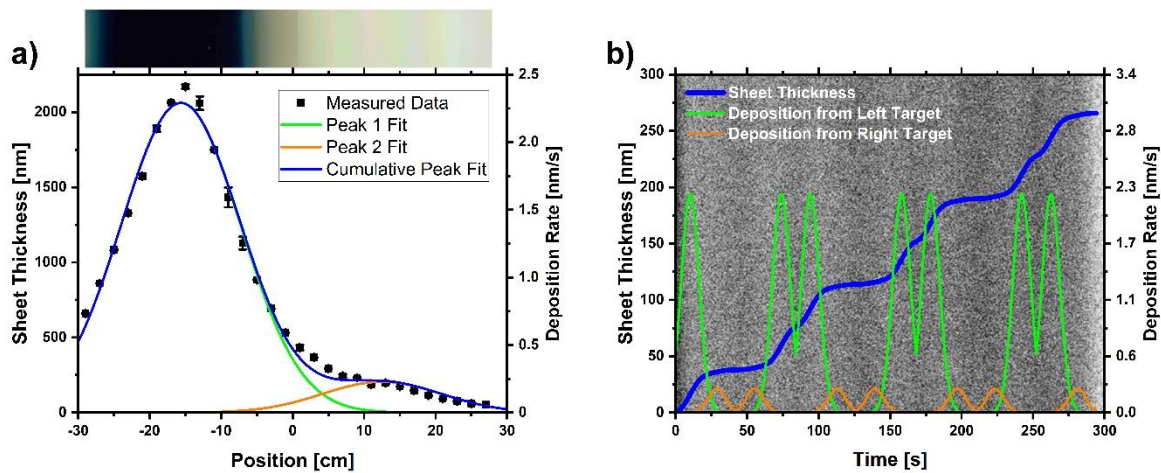F-STEM image from Figure 6-2 can be seen. Here, the glass substrate is on the left side and the platinum layer on the right side.

Figure 6-4a shows the measured thickness and the corresponding deposition rate of the static sample with respect to the position inside the chamber. To the left of -29 cm and to the right of 29 cm, the chamber wall blocks further deposition. The deposition rate in the black area is higher than at the other parts of the sample. The fitted deposition rates are used to calculate the layer growth of the dynamic sample as a function of time, see Figure **6-4**b. It can clearly be seen that the layer grows most during the periods in front of the left target. In addition, the dark areas of the HAADF-STEM image correspond well to periods of lower deposition rate. These areas also have a lower titanium-oxygen ratio than the brighter areas, as indicated by the EDX measurements in Figure 6-2. To analyze how this structure affects the electrical properties, resistance measurements were taken at one-centimeter intervals over the entire static sample. The resistivity of the dynamic sample was also determined.
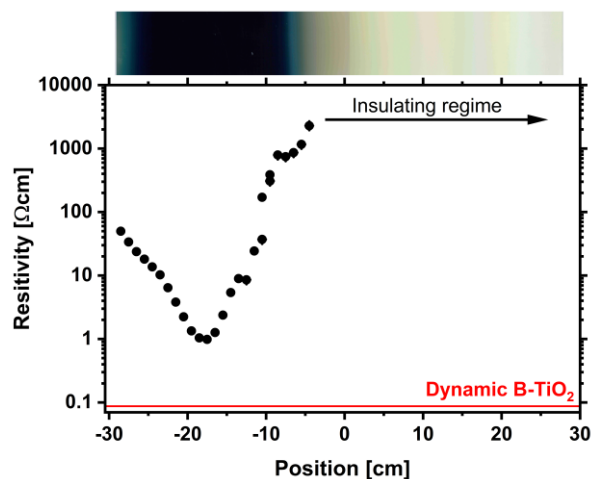
Figure 6-5: Resistivity measurements of the static sample at different positions. The inserted red line shows
the measured resistivity of the dynamic sample. For a better illustration, an image of the static
sample is shown above the graph.

Figure 6-5 shows the resistivity measured with a 4-point probe, at different positions along
the static sample. The point with the lowest resistivity corresponds well with the center of
the black area. For positions to the right of -5 cm, the resistivity was too high to be meas-
ured. Interestingly, the resistivity of the 250 nm dynamic sample (red solid line in Figure
6-5) is an order of magnitude lower than that of the static sample.

To analyze the structural composition of the static sample, Raman measurements were per-
formed for each centimeter of the static sample. A compilation of all Raman spectra can be
found in the supplementary information (S-6-Gif1). Figure 6-6 shows the Raman spectra
for four selected positions, that are representative for their surrounding areas.
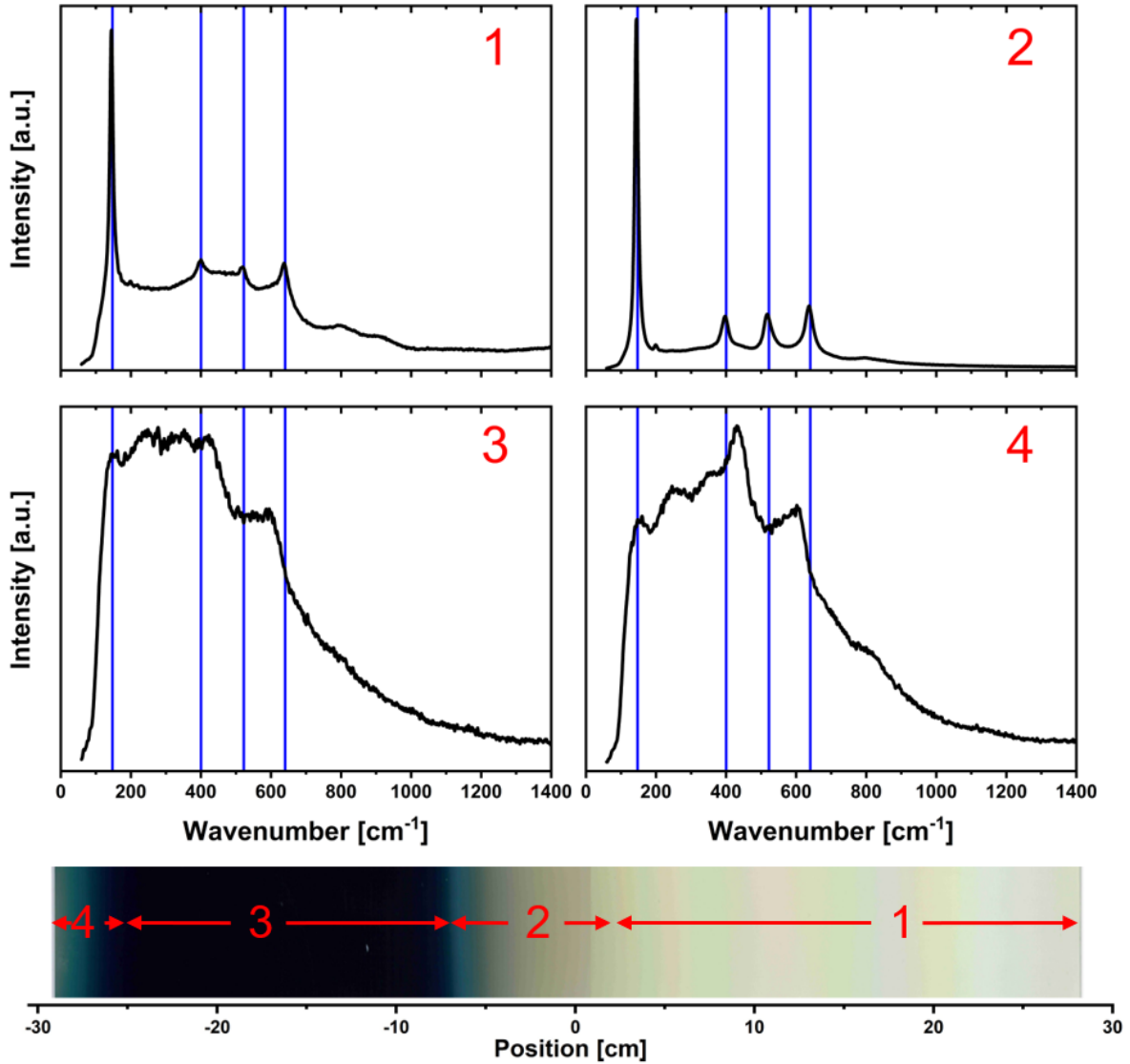
Figure 6-6: Raman spectra for four selected positions of the static sample. The numbers represent the corresponding position on the sample. The positions can be seen in the image of the sample. The arrows symbolize the range in which the Raman signal is comparable. The blue vertical lines show the wavenumbers for anatase TiO_2 peaks (147 cm^{-1}, 400 cm^{-1}, 522 cm^{-1}, 640 cm^{-1}).

The four points of interest are located in front of the right target (1), between the two targets in the transparent area (2), in the center of the black area (3), and to the left of the black area (4). Spectrum 1 shows peaks corresponding to anatase TiO_2 structures, while at the same time an amorphous background was observed. Between the two targets (Spectrum 2), the anatase peaks are more easily distinguished from the amorphous background. The sample is also thicker than at point 1. In the black area (spectrum 3), only the anatase peak at 147 cm^{-1} remains distinguishable. The amorphous background here is very dominant. However, to the left of the black area (Spectrum 4), new peaks appear next to the 147 cm^{-1} anatase peak. These peaks are at 247 cm^{-1}, 435 cm^{-1} and 602 cm^{-1} and cannot be assigned

to the anatase phase of TiO_2. However, due to the broad nature of the peaks, the possible existence of several other crystal structures cannot be excluded. As can be seen from the EDX measurements shown in Figure 6-2, the region studied exhibits a reduced chemical phase identified as the Magneli phases (Ti_nO_{2n-1}, where n is an integer). The exact enumeration of these phases remains elusive, although preparations and analyses have been extended up to n = 20. [189] Notable examples include Ti_2O_3, Ti_3O_5 and Ti_4O_7, which have been extensively studied. [190] These Magneli phases exhibit superior electrical conductivity compared to stoichiometric TiO2 and other Magneli phases with higher values of n. Magneli phases with n $\leq$ 4 prove to be promising catalysts, exhibiting enhanced catalytic activity, remarkable stability and resistance to corrosion. Conversely, for n > 4, substantial changes in the crystal structures lead to notable shifts in the catalytic properties. [191,192] Raman studies of Ti_2O_3, Ti_3O_5 and Ti_4O_7 show a variety of peaks for each phase. [193–195] The congruence in peak positions between these studies and the broad peaks observed in Figure 6-6 supports the presence of these three Magneli phases in the sample investigated. However, the absence of an identifiable dominant phase necessitates the assumption of a composite mixture consisting of these three distinct phases.

X-ray diffraction (XRD) analyses performed on the dynamic sample indicated the absence of a dominant crystal structure, as corroborated by the Raman spectroscopic measurements presented here. [187]

The compilation S-6-Gif1 in the supplementary information shows the Raman spectrum for each point of the sample. There it can also be seen that the transition from the gray to the black area is accompanied by a transition from a crystalline to an amorphous structure. The same transition can be seen on the left side of the black area.

To understand the influence of the single phases towards the enhanced photoelectrochemical activity of the dynamic sample, linear sweep voltammetry measurements (LSV) were done on each centimeter of the static sample as well as on the dynamic sample. The active area was a circle with 1 cm diameter. In that way each spot of the static sample can be measured. The measurements at 1 sun and in darkness are shown in Figure 6-7 and Figure 6-8, respectively. The position of the measurements shown in the graph correspond to the center of the active area.
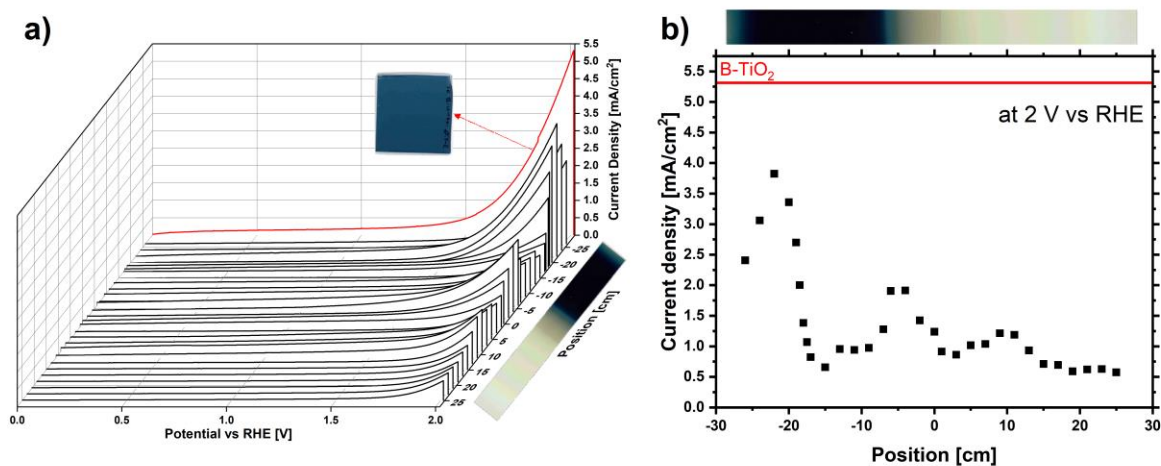
Figure 6-7: Linear Sweep Voltammetry. a) LSV of different positions of the static sample under 1 sun illumination. For a better visualization, an image of the sample is shown next to the corresponding positions. The red line shows the LSV measurement for the dynamic sample. Next to the red line an image of the dynamic sample is shown. b) Current densities measured by LSV at 2 V vs RHE for each centimeter of the static sample. The red line shows the current density of the dynamic sample. For better visualization an image of the static sample is shown above the graph.

The red curve in Figure 6-7a represents the LSV for the dynamic sample and the black lines are the LSV measurements for each centimeter of the static sample. Additionally, Figure 6-7b shows the current densities measured at 2 V vs. RHE. While the dynamic sample (red curves) shows the highest current density, two regions of the static sample also show remarkably high current densities. These two areas are located at the edge of the crystallin and amorphous regions, as shown by the Raman measurements. However, the regions do not have the same maximum photocurrent densities. The photocurrent to the left of the black region is higher. This can be explained by the different crystal structures at these positions. While the Raman spectrum of the region to the right of the black region shows an anatase crystal structure, the position to the left of the black region consists of Ti_3O_5 phases. These crystal structures are known for their enhanced photoelectrochemical performance compared to pristine TiO_2.[196] However, this does not explain the enhanced photocurrent of the dynamic sample. Lü et al. investigated a similar behavior in nanoparticles of B-TiO_2.[188] They studied the interface of the crystalline core with the amorphous shell in order to understand the improved conductivity, compared to pristine anatase nanoparticles. To do this, they created TiO_2 homojunction films consisting of an oxygen-deficient amorphous layer on top. They found that metallic conduction is enabled at the interface, where band bending occurs due to different positions of the Fermi level relative to the conduction band. This leads to an accumulation of electrons at the interface of the crystalline side, resulting in a high interfacial carrier concentration. They conclude this to be the

reason for the enhanced electron transport of B-TiO₂. The Raman measurement shown in this article suggest a similar behavior, which would explain the enhanced conductivity and photocurrent of the dynamic sample.

Figure 6-8 shows the LSV measurements without illumination. The influence on the photoinduced carriers can be seen here.
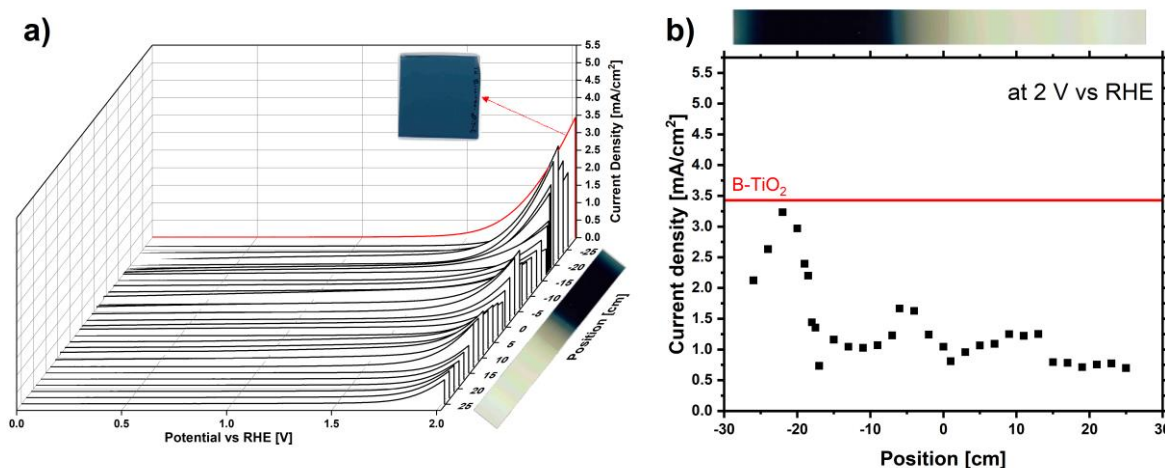
Figure 6-8: Linear Sweep Voltammetry without illumination. a) LSV on different positions of the static sample. For better visualization, an image of the sample is shown next to the corresponding positions. The red line shows the LSV measurement for the dynamic sample. Next to the red line an image of the dynamic sample is shown. b) Current densities measured by LSV at 2 V vs RHE for different positions of the static sample. The red line shows the current density for the dynamic sample. An image of the static sample is shown above the graph.

The LSV measurements of the static sample in the dark show a similar pattern to the measurements under illumination. Two areas of increased current density are located at the edges of the black region, the same as for the measurement under illumination. While the current densities observed at the peak positions of -5 cm and 10 cm show an approximate equivalence between measurements carried out under illuminated and dark conditions, a noticeable divergence appears at the -21 cm position, where the current density significantly exceeds that observed in the dark. This observed phenomenon can be attributed to the presence of several Magneli phases in this region of the sample, which exhibit enhanced photocatalytic activity in contrast to the predominant TiO₂ phase observed in other regions of the sample. Consequently, the enhanced water splitting activity catalysed by the Magneli phases is shown as an increased current density under illumination conditions.

However, as shown in Figure 6-8b, the current density of the dynamic sample at 2 V vs. RHE is not increased compared to the static sample. Moreover, it is in good agreement

with the highest current density of the static sample. The difference in current density between illumination and darkness is by far the largest for the dynamic sample. This alternating crystalline and amorphous phases might lead to an enhanced extraction of the photo-generated charge carriers, as explained above. The individual positions on the static sample, especially in the black area, don't have this effect and therefore show a reduced photoelectrochemical behavior.

Direct comparison with other publications is difficult. However, to get the results of this work into context, two comparable samples for literature are taken exemplary. Liang et al. sputtered an amorphous black TiO_2:H thin film and achieved a saturated current density of 0.67 mA/cm^2 at 1.23 V vs RHE with 1M NaOH as electrolyte under AM 1.5 irradiation.[186] Cho et al. created multiple heterojunctions of crystalline anatase / disordered rutile / ordered rutile layers within a single TiO_2 nanoparticle. Using this method, they achieved a current density of 1 mA/cm^2 at 1.9 V vs. RHE with 1M KOH as electrolyte under irradiation of 1 sun.[197] However, the photocurrent density of 5.26 mA/cm^2 at 2 V vs. RHE, of the dynamic sample shown in this work is significantly higher.

6.5 Conclusion

In this work, the influence of the dynamic nature of an asymmetric bipolar magnetron sputter processes on the growth of B-TiO_2 is studied, aiming to understand its enhanced photoelectrochemical activity. In order to study the layered structure of the dynamically sputtered films, static sputtering was used to analyze the individual phases.

It was found that the asymmetric process mainly leads to two distinct phases, a low light-absorbing crystalline and phase and a high light-absorbing amorphous phase. We show, that the dynamically sputtered sample exhibits superior photoelectrochemical properties compared to any of the individual phases from the static process. Notably, the electrical resistivity decreased by a factor of 10, accompanied by a substantial increase in the measured current during photoelectrochemical water splitting. This enhancement is most likely attributed to an improved extraction of photogenerated charge carriers at the amorphous/crystalline interface. This behavior was also described in the context of B-TiO_2 core-shell nanoparticles. Consequently, the findings presented in this article mark a significant step toward the development of large-area B-TiO_2 thin films with enhanced capabilities for photoelectrochemical water splitting and thereby fostering progress in sustainable energy technologies.

6.6 Acknowledgments

6.7 Supporting Information

Compilation of all Raman spectra

7.   Summary & Conclusion

The aim of this work was to study the cause of the significantly enhanced photoelectro-chemical water splitting activity of a novel B-TiO$_2$ thin film photoanode. The thin film was prepared by a newly developed sputtering process. In this dissertation, various aspects of the new B-TiO$_2$ thin film have been thoroughly examined. Topics covered include the fundamental optical, electrical and morphological properties of the film, the modelling of the defect and band structure, and a detailed analysis of the growth of the film.

To comprehend the enhanced water splitting activity, the optical and electrical properties of the film were first studied. It was shown that small changes in the power distribution to the two titanium targets in the newly developed asymmetric bipolar reactive magnetron sputtering process drastically change the optoelectronic properties. As the power is concentrated on one target, the electrical conductivity and light absorption increase continuously. Thus, the enhanced light absorption allows more electron-hole pairs to be generated, which in turn allows more water splitting reactions to take place. In addition, the improved electrical conductivity decreases recombination by allowing faster electron transport. However, this does not explain why the highest current density during the water splitting reaction was measured at a DC of 75%.

In order to understand this phenomenon in detail, a fine tuning of the duty cycle steps was carried out. This was accompanied by detailed optical, electrical and structural characterisation. The evaluations of reflectance (R) and transmittance (T) showed a continuous decrease in transmittance with increasing duty cycle while maintaining a constant film thickness. In contrast, the reflectance did not show a clear trend. It decreased steadily below 800 nm and increased steadily above 800 nm with increasing duty cycle. The calculated absorption (1-R-T) profiles showed a progressive increase in optical absorption, peaking at a duty cycle of 77%. Below 800 nm, the absorption continued to increase while it decreased for wavelengths above 800 nm. The dark conductivity measurements showed an exponential enhancement with an increasing duty cycle. A significant increase in conductivity occurred primarily in samples with a duty cycle greater than 75%.

The measured optical data was used to construct a composite model that integrates the O'Leary-Johnson-Lim (OJL) and Drude-Lorentz models. The Drude-Lorentz model was used to determine the plasma frequency, which is directly related to the defect density within the sample. The defect density showed an incremental trend up to a DC of 75%, after which it reached a plateau. This explains the increase in absorption and electrical conductivity up to DC=75%. However, subsequent observations prompted the exploration of an additional parameter derived from the OJL model. The gamma function, which characterises the state of the band tails within the band gap, has been considered. A decreasing

value of this parameter indicates a convergence of the band tails. A correlation was found between the gamma function and the variation in duty cycle for the analysed samples. The gamma function remained stable up to a DC of 75% before decreasing, with minimal changes observed for DC > 79%. The optical models provided insights into why the optimal water splitting activity occurred at a duty cycle of 75%. Up to this point, the defect density increased continuously, resulting in higher light absorption and electrical conductivity. XPS measurements identified the presence of Ti^{3+} states, which are considered beneficial for photoelectrochemical water splitting.[198–200] The improvements in optoelectrical properties persist beyond a 75% duty cycle, where the defect density reaches a plateau. This suggests a shift in state localization, supported by the decreasing gamma function. The Ti^{3+} states have been energetically repositioned deeper within the band gap, resulting in its narrowing. However, this altered energetic configuration reduces the measured current during photoelectrochemical water splitting, as fewer reactions occur due to the corresponding shift in energetics.

The sputtering process used to create the B-TiO$_2$ thin films is inherently dynamic. The substrate moves back and forth in front of the targets rather than maintaining a static position. Usually, this dynamic configuration ensures homogeneity in the growth of films, reducing local variations in growth rate that could otherwise affect the entire film. However, the process described in this study is asymmetric. This means that the two titanium targets yield different material compositions. As a result, the lateral growth of the sample is inhomogeneous. The final sample is therefore made up of several superimposed layers with different proportions of titanium and oxygen atoms. To comprehend the implications of this non-uniform structure, a static version of the process was performed. In this setup, the substrate remained stationary, completely covering the entire chamber, which allowed for the analysis of temporal growth with spatial resolution. Examination of individual points within the static sample revealed two primary regions: a black region characterised by an exceptionally high growth rate, close to the target with the higher applied power (75%), and a transparent region with a significantly reduced growth rate, close to the target with the lower applied power (25%). The region between the two targets appears to have a slight brownish tint, and there is a gradual transition from the transparent to the black region.

The analysis of the crystalline structure indicates that the transparent region is primarily composed of anatase TiO$_2$, while the black region lacks a dominant crystalline structure and can be classified as amorphous. The transition between these two phases is sharp. Similar to the B-TiO$_2$ nanoparticles, the sputtered samples also display two distinct regions of crystalline and amorphous phases, which are clearly distinguishable from each other.

Regarding electrical characterisation, the black area of the stationary sample exhibits a significantly lower electrical resistance than the transparent area. Notably, the electrical resistance of the dynamic sample is ten times lower than the most conductive point of the static sample. This phenomenon has been attributed to the presence of a conduction channel at the interface between the crystalline and amorphous phases. The improved efficiency of B-TiO$_2$ nanoparticles has also been explained by this feature. The conduction channel facilitates the flow of charge carriers, contributing to the increased conductivity observed in the dynamic sample. To analyse the influence of these properties on water splitting activity, the static samples underwent photoelectrochemical analysis. The results indicate that the highest current was measured at the edges of the black phase, with the maximum current occurring on the side farthest from the target with the lower applied power (see Figure 6-7 for a better visualisation). Ti$_2$O$_3$ crystal structures were identified at these locations, which are known to have enhanced photoelectrochemical activity compared to TiO$_2$. The dynamic sample exhibited a significantly higher current than the static sample at these points. This is likely due to the presence of the conduction channel in the dynamic sample allowing more effective extraction of carriers generated by light absorption, thereby contributing to the enhanced water splitting activity. The statement is supported by photoelectrochemical measurements performed without illumination. The measured current density of the dynamic sample closely matches the highest current densities measured in the static sample.

This work presents the preparation and study of a TiO$_2$-based thin film photoanode for green hydrogen production. The newly developed sputtering process is capable of producing highly efficient B-TiO$_2$ photoanodes. Notably, the photoelectrochemical water splitting activity of these sputtered films surpasses that of other comparable B-TiO$_2$ thin films and nanoparticles. This achievement contributes significantly to the development of sustainable energy sources and emphasises the importance of photoelectrochemical water splitting in the future hydrogen economy. The process demonstrated is also suitable for the scalable production of large-area B-TiO$_2$ thin-film photoanodes. This achievement provides a promising basis for a convenient and cost-effective method that will facilitate the widespread practical use of B-TiO$_2$ in various applications.

References

[1] High Representative of the Union for Foreign Affairs and Security Policy, *JOINT COMMUNICATION TO THE EUROPEAN PARLIAMENT, THE COUNCIL, THE EUROPEAN ECONOMIC AND SOCIAL COMMITTEE AND THE COMMITTEE OF THE REGIONS: EU external energy engagement in a changing world* **2022**, https://eur-lex.europa.eu/legal-content/EN/TXT/PDF/?uri=CELEX:52022JC0023.

[2] Deutscher Bundestag - Wissenschaftliche Dienste, *Die Energieaußenpolitik der Europäischen Union*, https://www.bundestag.de/resource/blob/498000/56ab0ba5c4c628b4eac40b550039e222/Die-Energieaussenpolitik-der-Europaeischen-Union-data.pdf.

[3] D. Bogdanov, M. Ram, A. Aghahosseini, A. Gulagi, A. S. Oyewo, M. Child, U. Caldera, K. Sadovskaia, J. Farfan, L. de Souza Noel Simas Barbosa, M. Fasihi, S. Khalili, T. Traber, C. Breyer, *Energy* **2021**, *227*, 120467.

[4] European Commission, *REPowerEU: A plan to rapidly reduce dependence on Russian fossil fuels and fast forward the green transition*, https://ec.europa.eu/commission/presscorner/detail/en/IP_22_3131.

[5] European Comission, *COMMUNICATION FROM THE COMMISSION TO THE EUROPEAN PARLIAMENT, THE EUROPEAN COUNCIL, THE COUNCIL, THE EUROPEAN ECONOMIC AND SOCIAL COMMITTEE, THE COMMITTEE OF THE REGIONS AND THE EUROPEAN INVESTMENT BANK: A Clean Planet for all A European strategic long-term vision for a prosperous, modern, competitive and climate neutral economy.*

[6] G. Herrera-Franco, H. A. Bollmann, J. C. Pasqual Lofhagen, Bravo-Montero, P. Carrión-Mero, *Environmental Development* **2023**, *46*, 100858.

[7] E. R. Bandala, M. Berli, *Materials Science for Energy Technologies* **2019**, *2*, 29.

[8] A. Saravanan, P. S. Kumar, D.-V. N. Vo, P. R. Yaashikaa, S. Karishma, S. Jeevantham, B. Gayathri, V. D. Bharathi, *Environ Chem Lett* **2021**, *19*, 441.

[9] R. van de Krol, B. A. Parkinson, *MRS Energy and Sustainability* **2017**, *4*.

[10] A. Fujishima, K. Honda, *Nature* **1972**, *238*, 37.

[11] S. A. Rawool, K. K. Yadav, V. Polshettiwar, *Chemical science* **2021**, *12*, 4267.

[12] H. W. S. Barros, D. A. Duarte, J. C. Sagás, *Thin Solid Films* **2020**, *696*, 137762.

[13] F. Li, Y. Huang, H. Peng, Y. Cao, Y. Niu, *International Journal of Photoenergy* **2020**, *2020*, 1.

[14] Radhika V Nair,Venkata Siva Gummaluri,Murukeshan Vadakke Matham,Vijayan C.

[15] A. Brudnik, H. Czternastek, K. Zakrzewska, M. Jachimowski, *Thin Solid Films* **1991**, *199*, 45.

[16] O. Banakh, P. E. Schmid, R. Sanjinés, F. Lévy, *Surface and Coatings Technology* **2002**, *151-152*, 272.

[17] X. Chen, L. Liu, P. Y. Yu, S. S. Mao, *Science* **2011**, *331*, 746.

[18] A. Chatzitakis, S. Sartori, *Chemphyschem* **2019**, *20*, 1272.

[19] X. Liu, G. Zhu, X. Wang, X. Yuan, T. Lin, F. Huang, *Advanced Energy Materials* **2016**, *6*.

[20] M. Tian, C. Liu, J. Ge, D. Geohegan, G. Duscher, G. Eres, *Journal of Materials Research* **2019**, *34*, 1138.

[21] J. Gao, Q. Shen, R. Guan, J. Xue, X. Liu, H. Jia, Q. Li, Y. Wu, *Journal of CO2 Utilization* **2020**, *35*, 205.

[22] M. Ismael, *Solar Energy* **2020**, *211*, 522.

[23] P. Puranen, A. Kosonen, J. Ahola, *Solar Energy* **2021**, *213*, 246.

[24] P. Gabrielli, A. Poluzzi, G. J. Kramer, C. Spiers, M. Mazzotti, M. Gazzani, *Renewable and Sustainable Energy Reviews* **2020**, *121*, 109629.

[25] C. Loschan, D. Schwabeneder, M. Maldet, G. Lettner, H. Auer, *Energies* **2023**, *16*, 5333.

[26] G. Pagani, Y. Hajimolana, C. Acar, *International Journal of Hydrogen Energy* **2024**, *52*, 418.

[27] W. Liu, H. Zuo, J. Wang, Q. Xue, B. Ren, F. Yang, *International Journal of Hydrogen Energy* **2021**, *46*, 10548.

[28] European Comission, *COMMUNICATION FROM THE COMMISSION TO THE EUROPEAN PARLIAMENT, THE COUNCIL, THE EUROPEAN ECONOMIC AND SOCIAL COMMITTEE AND THE COMMITTEE OF THE REGIONS: A hydrogen strategy for a climate-neutral Europe*.

[29] S. van Renssen, *Nature Climate Change* **2020**, *10*, 799.

[30] D. A. Crowl, Y.-D. Jo, *Journal of Loss Prevention in the Process Industries* **2007**, *20*, 158.

[31] W. D. Sproul, D. J. Christie, D. C. Carter, *Thin Solid Films* **2005**, *491*, 1.

[32] K. Seshan (Ed.), *Handbook of thin-film deposition processes and techniques: Principles, methods, equipment and applications*, Noyes Publications/William Andrew Pub, Norwich, N.Y **2002**.

[33] V. S. Smentkowski, *Progress in Surface Science* **2000**, *64*, 1.

[34] P. Sigmund, *1437-0859* **1981**, *47*, 9.

[35] P. Kelly, R. Arnell, *Vacuum* **2000**, *56*, 159.

[36] S. Swann, *Physics in Technology* **1988**, *19*, 67.

[37] G. Bräuer, B. Szyszka, M. Vergöhl, R. Bandorf, *Vacuum* **2010**, *84*, 1354.

[38] K. Strijckmans, R. Schelfhout, D. Depla, *Journal of Applied Physics* **2018**, *124*.

[39] D. Depla, S. Mahieu (Eds.), *Reactive sputter deposition*, Springer, Berlin, Heidelberg **2008**.

[40] I. Safi, *Surface and Coatings Technology* **2000**, *127*, 203.

[41] J. Musil, P. Baroch, J. Vlček, K. H. Nam, J. G. Han, *Thin Solid Films* **2005**, *475*, 208.

[42] J. T. Gudmundsson, *Plasma Sources Sci. Technol.* **2020**, *29*, 113001.

[43] J. Li, G.-K. Ren, J. Chen, X. Chen, W. Wu, Y. Liu, X. Chen, J. Song, Y.-H. Lin, Y. Shi, *JOM* **2022**, *74*, 3069.

[44] J. Li, G.-K. Ren, J. Chen, X. Chen, W. Wu, Y. Liu, X. Chen, J. Song, Y.-H. Lin, Y. Shi, *JOM* **2022**, *74*, 3069.

[45] J. Sellers, *Surface and Coatings Technology* **1998**, *98*, 1245.

[46] C. Ros, T. Andreu, J. R. Morante, *J. Mater. Chem. A* **2020**, *8*, 10625.

[47] M. G. Walter, E. L. Warren, J. R. McKone, S. W. Boettcher, Q. Mi, E. A. Santori, N. S. Lewis, *Chemical reviews* **2010**, *110*, 6446.

[48] S. Nishioka, F. E. Osterloh, X. Wang, T. E. Mallouk, K. Maeda, *Nat Rev Methods Primers* **2023**, *3*, 1.

[49] C. Kranz, M. Wachtler, *Chemical Society reviews* **2021**, *50*, 1407.

[50] B. J. Ng, L. K. Putri, X. Y. Kong, Y. W. Teh, P. Pasbakhsh, S. P. Chai, *Advanced science* **2020**, *7*, 1903171.

[51] Z. Zhang, Yates, J. T., Jr., *Chemical reviews* **2012**, *112*, 5520.

[52] N. S. Hassan, A. A. Jalil, N. F. Khusnun, A. Ahmad, T. A. T. Abdullah, R. M. Kasmani, N. Norazahar, M. F. A. Kamaroddin, D. V. N. Vo, *Environmental Chemistry Letters* **2021**.

[53] A. J. Bard, L. R. Faulkner, *Electrochemical methods: Fundamentals and applications*, Wiley, New York, Weinheim **2001**.

[54] P. Zhang, T. Wang, J. Gong, *Chem* **2018**, *4*, 223.

[55] C. Jiang, S. J. A. Moniz, A. Wang, T. Zhang, J. Tang, *Chemical Society reviews* **2017**, *46*, 4645.

[56] C. Bie, L. Wang, J. Yu, *Chem* **2022**, *8*, 1567.

[57] J. Qi, W. Zhang, R. Cao, *Advanced Energy Materials* **2018**, *8*, 1701620.

[58] C. Ding, J. Shi, Z. Wang, C. Li, *ACS Catalysis* **2016**, *7*, 675.

[59] Y. Liang, G. Huang, X. Xin, Y. Yao, Y. Li, J. Yin, X. Li, Y. Wu, S. Gao, *Journal of Materials Science & Technology* **2022**, *112*, 239.

[60] L. Andronic, A. Enesca, *Front. Chem.* **2020**, *8*, 565489.

[61] A. Naldoni, M. Allieta, S. Santangelo, M. Marelli, F. Fabbri, S. Cappelli, C. L. Bianchi, R. Psaro, V. Dal Santo, *Journal of the American Chemical Society* **2012**, *134*, 7600.

[62] S. Lettieri, M. Pavone, A. Fioravanti, L. Santamaria Amato, P. Maddalena, *Materials (Basel)* **2021**, *14*.

[63] D.-H. Yoon, M. R. U. D. Biswas, A. Sakthisabarimoorthi, *Optical Materials* **2022**, *133*, 113030.

[64] M. Soleimani, J. B. Ghasemi, A. Badiei, *Inorganic Chemistry Communications* **2022**, *135*.

[65] S. Kim, Y. Cho, R. Rhee, J. H. Park, *Carbon Energy* **2020**, *2*, 44.

[66] A. Balog, G. F. Samu, S. Peto, C. Janaky, *ACS Mater Au* **2021**, *1*, 157.

[67] D. V. Zyabkin, H. P. Gunnlaugsson, J. N. Gonçalves, K. Bharuth-Ram, B. Qi, I. Unzueta, D. Naidoo, R. Mantovan, H. Masenda, S. Ólafsson, G. Peters, J. Schell, U. Vetter, A. Dimitrova, S. Krischok, P. Schaaf, *The Journal of Physical Chemistry C* **2020**, *124*, 7511.

[68] B. Wang, S. Shen, S. S. Mao, *Journal of Materiomics* **2017**, *3*, 96.

[69] Z. Li, H. Bian, X. Xiao, J. Shen, C. Zhao, J. Lu, Y. Y. Li, *ACS Applied Nano Materials* **2019**, *2*, 7372.

[70] H. Jaafar, M. F. Ain, Z. A. Ahmad, *Opt Quant Electron* **2020**, *52*, 1.

[71] S. Namboorimadathil Backer, A. M. Ramachandran, A. A. Venugopal, A. P. Mohamed, A. Asok, S. Pillai, *ACS Appl. Nano Mater.* **2020**, *3*, 6827.

[72] I. Zada, W. Zhang, P. Sun, M. Imtiaz, N. Iqbal, U. Ghani, R. Naz, Y. Zhang, Y. Li, J. Gu, Q. Liu, D. Pantelić, B. Jelenković, Di Zhang, *Applied Materials Today* **2020**, *20*, 100669.

[73] Y. Yang, M. R. Hoffmann, *Environmental science & technology* **2016**, *50*, 11888.

[74] B. Ou, J. Wang, Y. Wu, S. Zhao, Z. Wang, *ACS Omega* **2019**, *4*, 9664.

[75] D. S. Kim, D. J. Chung, J. Bae, G. Jeong, H. Kim, *Electrochimica Acta* **2017**, *258*, 336.

[76] T. Wu, G. Sun, W. Lu, L. Zhao, A. Mauger, C. M. Julien, L. Sun, H. Xie, J. Liu, *Electrochimica Acta* **2020**, *353*, 136529.

[77] W. Ren, Y. Yan, L. Zeng, Z. Shi, an Gong, P. Schaaf, D. Wang, J. Zhao, B. Zou, H. Yu, G. Chen, E. M. B. Brown, A. Wu, *Advanced healthcare materials* **2015**, *4*, 1526.

[78] W. Ni, M. Li, J. Cui, Z. Xing, Z. Li, X. Wu, E. Song, M. Gong, W. Zhou, *Materials science & engineering. C, Materials for biological applications* **2017**, *81*, 252.

[79] W. Zhang, J. Gu, K. Li, J. Zhao, H. Ma, C. Wu, C. Zhang, Y. Xie, F. Yang, X. Zheng, *Materials science & engineering. C, Materials for biological applications* **2019**, *102*, 458.

[80] X. Chen, L. Liu, Z. Liu, M. A. Marcus, W.-C. Wang, N. A. Oyler, M. E. Grass, B. Mao, P.-A. Glans, P. Y. Yu, J. Guo, S. S. Mao, *Sci Rep* **2013**, *3*, 1510.

[81] L. Liu, P. Y. Yu, X. Chen, S. S. Mao, D. Z. Shen, *Phys Rev Lett* **2013**, *111*, 65505.

[82] R. Katal, M. Salehi, M. H. Davood Abadi Farahani, S. Masudy-Panah, S. L. Ong, J. Hu, *ACS applied materials & interfaces* **2018**, *10*, 35316.

[83] X. Zhang, M. Cai, N. Cui, G. Chen, G. Zou, L. Zhou, *Nanomaterials* **2021**, *11*, 2648.

[84] G. Li, Z. Lian, X. Li, Y. Xu, W. Wang, D. Zhang, F. Tian, H. Li, *J. Mater. Chem. A* **2015**, *3*, 3748.

[85] Y. Ishida, W. Doshin, H. Tsukamoto, T. Yonezawa, *Chem. Lett.* **2015**, *44*, 1327.

[86] F. Teng, M. Li, C. Gao, G. Zhang, P. Zhang, Y. Wang, L. Chen, E. Xie, *Applied Catalysis B: Environmental* **2014**, *148-149*, 339.

[87] T. Jedsukontorn, T. Ueno, N. Saito, M. Hunsom, *Journal of Alloys and Compounds* **2017**, *726*, 567.

[88] M. Ye, J. Jia, Z. Wu, C. Qian, R. Chen, P. G. O'Brien, W. Sun, Y. Dong, G. A. Ozin, *Advanced Energy Materials* **2017**, *7*.

[89] G. Zhu, J. Xu, W. Zhao, F. Huang, *ACS applied materials & interfaces* **2016**, *8*, 31716.

[90] X. Zhang, M. Cai, N. Cui, G. Chen, G. Zou, L. Zhou, *Nanomaterials (Basel)* **2021**, *11*.

[91] S. Chen, Y. Xiao, Y. Wang, Z. Hu, H. Zhao, W. Xie, *Nanomaterials (Basel)* **2018**, *8*.

[92] M. S. Dresselhaus, I. L. Thomas, *Nature* **2001**, *414*, 332.

[93] T. Hisatomi, J. Kubota, K. Domen, *Chemical Society reviews* **2014**, *43*, 7520.

[94] Y. Tachibana, L. Vayssieres, J. R. Durrant, *Nature Photonics* **2012**, *6*, 511.

[95] S. Ardo, D. Fernandez Rivas, M. A. Modestino, V. Schulze Greiving, F. F. Abdi, E. Alarcon Llado, V. Artero, K. Ayers, C. Battaglia, J.-P. Becker, D. Bederak, A. Berger, F. Buda, E. Chinello, B. Dam, V. Di Palma, T. Edvinsson, K. Fujii, H. Gardeniers, H. Geerlings, S. M. H. Hashemi, S. Haussener, F. Houle, J. Huskens, B. D. James, K. Konrad, A. Kudo, P. P. Kunturu, D. Lohse, B. Mei, E. L. Miller, G. F. Moore, J. Muller, K. L. Orchard, T. E. Rosser, F. H. Saadi, J.-W. Schüttauf, B. Seger, S. W. Sheehan, W. A. Smith, J. Spurgeon, M. H. Tang, R. van de Krol, P. C. K. Vesborg, P. Westerik, *Energy and Environmental Science* **2018**, *11*, 2768.

[96] J. Jian, G. Jiang, R. van de Krol, B. Wei, H. Wang, *Nano Energy* **2018**, *51*, 457.

[97] M. S. Prévot, K. Sivula, *The Journal of Physical Chemistry C* **2013**, *117*, 17879.

[98] B. Turan, J. P. Becker, F. Urbain, F. Finger, U. Rau, S. Haas, *Nature communications* **2016**, *7*, 12681.

[99] S. E. Hosseini, M. A. Wahid, *International Journal of Energy Research* **2020**, *44*, 4110.

[100] J. Nowotny, C. C. Sorrell, T. Bak, L. R. Sheppard, *Solar Energy* **2005**, *78*, 593.

[101] J. Highfield, *Molecules* **2015**, *20*, 6739.

[102] K. Sivula, R. van de Krol, *Nature Reviews Materials* **2016**, *1*.

[103] A. Grimm, W. A. de Jong, G. J. Kramer, *International Journal of Hydrogen Energy* **2020**, *45*, 22545.

[104] I. R. Hamdani, A. N. Bhaskarwar, *Renewable and Sustainable Energy Reviews* **2021**, *138*, 110503.

[105] E. B. Gracien, J. Shen, X. Sun, D. Liu, M. Li, S. Yao, J. Sun, *Thin Solid Films* **2007**, *515*, 5287.

[106]   S. Huo, Y. Wu, C. Zhao, F. Yu, J. Fang, Y. Yang, *Industrial & Engineering Chemistry Research* **2020**, *59*, 14224.

[107]   Y. J. Hwang, C. Hahn, B. Liu, P. Yang, *ACS nano* **2012**, *6*, 5060.

[108]   R. Li, Y. Weng, X. Zhou, X. Wang, Y. Mi, R. Chong, H. Han, C. Li, *Energy & Environmental Science* **2015**, *8*, 2377.

[109]   A. L. Linsebigler, G. Lu, J. T. Yates, *Chemical Reviews* **1995**, *95*, 735.

[110]   S. Shen, J. Chen, M. Wang, X. Sheng, X. Chen, X. Feng, S. S. Mao, *Progress in Materials Science* **2018**, *98*, 299.

[111]   A. Brudnik, A. Gorzkowska-Sobaś, E. Pamuła, M. Radecka, K. Zakrzewska, *Journal of Power Sources* **2007**, *173*, 774.

[112]   T. Berger, M. Sterrer, O. Diwald, E. Knozinger, D. Panayotov, T. L. Thompson, Yates, J. T., Jr., *The journal of physical chemistry. B* **2005**, *109*, 6061.

[113]   T. Bak, J. Nowotny, M. Rekas, C. C. Sorrell, *International Journal of Hydrogen Energy* **2002**, *27*, 991.

[114]   J. Nowotny, T. Bak, M. Nowotny, L. Sheppard, *International Journal of Hydrogen Energy* **2007**, *32*, 2609.

[115]   M. Radecka, M. Rekas, A. Trenczek-Zajac, K. Zakrzewska, *Journal of Power Sources* **2008**, *181*, 46.

[116]   H. Ennaceri, M. Boujnah, A. Taleb, A. Khaldoun, R. Sáez-Araoz, A. Ennaoui, A. El Kenz, A. Benyoussef, *International Journal of Hydrogen Energy* **2017**, *42*, 19467.

[117]   T. Lindgren, J. Lu, A. Hoel, C.-G. Granqvist, G. R. Torres, S.-E. Lindquist, *Solar Energy Materials and Solar Cells* **2004**, *84*, 145.

[118]   A. Li, Z. Wang, H. Yin, S. Wang, P. Yan, B. Huang, X. Wang, R. Li, X. Zong, H. Han, C. Li, *Chemical science* **2016**, *7*, 6076.

[119]   R. Yalavarthi, A. Naldoni, Š. Kment, L. Mascaretti, H. Kmentová, O. Tomanec, P. Schmuki, R. Zbořil, *Catalysts* **2019**, *9*, 204.

[120]   X. Chen, L. Liu, F. Huang, *Chemical Society reviews* **2015**, *44*, 1861.

[121]   A. Naldoni, M. Altomare, G. Zoppellaro, N. Liu, S. Kment, R. Zboril, P. Schmuki, *ACS Catal* **2019**, *9*, 345.

[122]   L. H. C. Amorin, L. Da Silva Martins, A. Urbano, C. S. dos Santos, R. Matos, M. V. Moro, T. F. Da Silva, C. L. Rodrigues, M. H. Tabacniks, *Journal of Materials Science: Materials in Electronics* **2019**, *31*, 1672.

[123]   J. Buha, *Journal of Physics D: Applied Physics* **2012**, *45*, 385305.

[124]   A. Nakaruk, C. Y. W. Lin, D. Channei, P. Koshy, C. C. Sorrell, *Journal of Sol-Gel Science and Technology* **2011**, *61*, 175.

[125]   A. A. Akl, H. Kamal, K. Abdel-Hady, *Applied Surface Science* **2006**, *252*, 8651.

[126]   S. B. Amor, L. Guedri, G. Baud, M. Jacquet, M. Ghedira, *Materials Chemistry and Physics* **2003**, *77*, 903.

[127] N. J. Suliali, W. E. Goosen, A. van Janse Vuuren, E. J. Olivier, B. Bakhit, H. Högberg, V. Darakchieva, J. R. Botha, *Vacuum* **2022**, *195*.

[128] A. Le Febvrier, L. Landälv, T. Liersch, D. Sandmark, P. Sandström, P. Eklund, *Vacuum* **2021**, *187*.

[129] D. Glöß, P. Frach, O. Zywitzki, T. Modes, S. Klinkenberg, C. Gottfried, *Surface and Coatings Technology* **2005**, *200*, 967.

[130] R. S. Santiago, L. C. D. Silva, F. D. Origo, C. Stegemann, I. L. Graff, R. G. Delatorre, D. A. Duarte, *Thin Solid Films* **2020**, *700*.

[131] H. Baránková, S. Berg, P. Carlsson, C. Nender, *Thin Solid Films* **1995**, *260*, 181.

[132] S. Berg, T. Nyberg, *Thin Solid Films* **2005**, *476*, 215.

[133] M. Radecka, A. Brudnik, K. Kulinowski, A. Kot, J. Leszczyński, J. Kanak, K. Zakrzewska, *Journal of Electronic Materials* **2019**, *48*, 5481.

[134] M. Radecka, A. Trenczek-Zajac, K. Zakrzewska, M. Rekas, *Journal of Power Sources* **2007**, *173*, 816.

[135] A. Belkind, Z. Zhao, R. Scholl, *Surface and Coatings Technology* **2003**, *163-164*, 695.

[136] P. Baroch, J. Musil, J. Vlcek, K. H. Nam, J. G. Han, *Surface and Coatings Technology* **2005**, *193*, 107.

[137] B. Bakhit, S. Mráz, J. Lu, J. Rosen, J. M. Schneider, L. Hultman, I. Petrov, G. Greczynski, *Vacuum* **2021**, *186*.

[138] X. Yuan, S. Liang, H. Ke, Q. Wei, Z. Huang, D. Chen, *Vacuum* **2020**, *172*.

[139] T. Miyagi, M. Kamei, T. Ogawa, T. Mitsuhashi, A. Yamazaki, T. Sato, *Thin Solid Films* **2003**, *442*, 32.

[140] P. Carlsson, C. Nender, H. Barankova, S. Berg, *Journal of Vacuum Science & Technology A: Vacuum, Surfaces, and Films* **1993**, *11*, 1534.

[141] N. Martin, C. Rousselot, C. Savall, F. Palmino, *Thin Solid Films* **1996**, *287*, 154.

[142] H. Zhu, E. Bunte, J. Hüpkes, S. M. Huang, *Thin Solid Films* **2011**, *519*, 2366.

[143] G. Balakrishnan, V. R. Bandi, S. M. Rajeswari, N. Balamurugan, R. V. Babu, J. I. Song, *Materials Research Bulletin* **2013**, *48*, 4901.

[144] T. Asanuma, T. Matsutani, C. Liu, T. Mihara, M. Kiuchi, *Journal of Applied Physics* **2004**, *95*, 6011.

[145] P. Makula, M. Pacia, W. Macyk, *The journal of physical chemistry letters* **2018**, *9*, 6814.

[146] K. Kollbek, M. Sikora, C. Kapusta, J. Szlachetko, K. Zakrzewska, K. Kowalski, M. Radecka, *Applied Surface Science* **2013**, *281*, 100.

[147] G. A. Tompsett, G. A. Bowmaker, R. P. Cooney, J. B. Metson, K. A. Rodgers, J. M. Seakins, *Journal of Raman Spectroscopy* **1995**, *26*, 57.

[148] F. Fabregat-Santiago, I. Mora-Seró, G. Garcia-Belmonte, J. Bisquert, *The Journal of Physical Chemistry B* **2002**, *107*, 758.

[149] G. Wang, H. Wang, Y. Ling, Y. Tang, X. Yang, R. C. Fitzmorris, C. Wang, J. Z. Zhang, Y. Li, *Nano letters* **2011**, *11*, 3026.

[150] H. Yao, J. Ma, Y. Mu, Y. Chen, S. Su, P. Lv, X. Zhang, D. Ding, W. Fu, H. Yang, *RSC Advances* **2015**, *5*, 6429.

[151] C.-J. Lin, W.-K. Tu, C.-K. Kuo, S.-H. Chien, *Journal of Power Sources* **2011**, *196*, 4865.

[152] N. Saranrom, T. Sintiam, R. Panyathip, K. Hongsith, S. Sucharitakul, A. Ngamjarurojana, D. Boonyawan, P. Kumnorkaew, T. Kerdcharoen, S. Choopun, *Phys. Status Solidi A* **2021**, *218*, 2000239.

[153] O. Ola, M. Maroto-Valer, *Journal of Photochemistry and Photobiology C: Photochemistry Reviews* **2015**, *24*, 16.

[154] K. Perović, F. M. dela Rosa, M. Kovačić, H. Kušić, U. Lavrenčič Štangar, F. Fresno, D. D. Dionysiou, A. L. Bozic, *Materials* **2020**, *13*, 1338.

[155] D. Berends, P. Schwager, K. Gehrke, M. Vehse, C. Agert, *Vacuum* **2022**, *203*, 111290.

[156] K. Zhang, L. Wang, J. K. Kim, M. Ma, G. Veerappan, C.-L. Lee, K. Kong, H. Lee, J. H. Park, *Energy Environ. Sci.* **2016**, *9*, 499.

[157] K. H. Kim, C.-W. Choi, S. Choung, Y. Cho, S. Kim, C. Oh, K.-S. Lee, C.-L. Lee, K. Zhang, J. W. Han, S.-Y. Choi, J. H. Park, *Advanced Energy Materials* **2022**, *12*, 2103495.

[158] G. Feng, M. Hu, S. Yuan, J. Nan, H. Zeng, *Nanomaterials (Basel)* **2021**, *11*.

[159] M. Pylnev, W.-H. Chang, M.-S. Wong, *Applied Surface Science* **2018**, *462*, 285.

[160] X. Yan, Y. Li, T. Xia, *International Journal of Photoenergy* **2017**, *2017*, 1.

[161] L. C. Escaliante, Pereira, Andre Luis de Jesus, L. J. Affonço, J. H. D. Da Silva, *Journal of Materials Research* **2021**, *36*, 3096.

[162] K. Zhang, J. H. Park, *The journal of physical chemistry letters* **2017**, *8*, 199.

[163] J. Jiang, Z. Xing, M. Li, Z. Li, X. Wu, M. Hu, J. Wan, N. Wang, A. S. Besov, W. Zhou, *Ind. Eng. Chem. Res.* **2017**, *56*, 7948.

[164] Z. Qiao, C. Agashe, D. Mergel, *Thin Solid Films* **2006**, *496*, 520.

[165] M. Kitano, M. Takeuchi, M. Matsuoka, J. M. Thomas, M. Anpo, *Chem. Lett.* **2005**, *34*, 616.

[166] J. Aljuaid, A. Timoumi, S. N. Alamri, *Optical Materials: X* **2022**, *16*, 100178.

[167] S. K. Mukherjee, D. Mergel, *Journal of Applied Physics* **2013**, *114*, 13501.

[168] M. M. Masayoshi Mikami, S. N. Shinichiro Nakamura, O. K. Osamu Kitao, H. A. Hironori Arakawa, X. G. Xavier Gonze, *Jpn. J. Appl. Phys.* **2000**, *39*, L847.

[169]   S. Boukrouh, R. Bensaha, S. Bourgeois, E. Finot, M. C. Marco de Lucas, *Thin Solid Films* **2008**, *516*, 6353.

[170]   B. Bharti, S. Kumar, H.-N. Lee, R. Kumar, *Sci Rep* **2016**, *6*, 32355.

[171]   X. Pan, M.-Q. Yang, X. Fu, N. Zhang, Y.-J. Xu, *Nanoscale* **2013**, *5*, 3601.

[172]   J. Boltz, D. Koehl, M. Wuttig, *Surface and Coatings Technology* **2010**, *205*, 2455.

[173]   R. Gouttebaron, D. Cornelissen, R. Snyders, J. P. Dauchot, M. Wautelet, M. Hecq, *Surface and Interface Analysis* **2000**, *30*, 527.

[174]   C. Di Valentin, G. Pacchioni, A. Selloni, *J. Phys. Chem. C* **2009**, *113*, 20543.

[175]   V. Pfeifer, P. Erhart, S. Li, K. Rachut, J. Morasch, J. Brötz, P. Reckers, T. Mayer, S. Rühle, A. Zaban, I. Mora Seró, J. Bisquert, W. Jaegermann, A. Klein, *The Journal of Physical Chemistry Letters* **2013**, *4*, 4182.

[176]   K. Pomoni, A. Vomvas, C. Trapalis, *Thin Solid Films* **2008**, *516*, 1271.

[177]   H. Tan, Z. Zhao, M. Niu, C. Mao, D. Cao, D. Cheng, P. Feng, Z. Sun, *Nanoscale* **2014**, *6*, 10216.

[178]   C. J. Dahlman, A. Agrawal, C. M. Staller, J. Adair, D. J. Milliron, *Chem. Mater.* **2019**, *31*, 502.

[179]   W. Rehm, R. Fischer, J. Stuke, H. Wagner, *Phys. Stat. Sol. (b)* **1977**, *79*, 539.

[180]   A.-M. Lepadatu, A. Slav, C. Palade, I. Dascalescu, M. Enculescu, S. Iftimie, S. Lazanu, V. S. Teodorescu, M. L. Ciurea, T. Stoica, *Sci Rep* **2018**, *8*, 4898.

[181]   L. Liao, M. Wang, Z. Li, X. Wang, W. Zhou, *Nanomaterials (Basel)* **2023**, *13*.

[182]   D.-H. Yoon, M. R. U. D. Biswas, A. Sakthisabarimoorthi, *Optical Materials* **2022**, *133*, 113030.

[183]   M. Tian, M. Mahjouri-Samani, G. Eres, R. Sachan, M. Yoon, M. F. Chisholm, K. Wang, A. A. Puretzky, C. M. Rouleau, D. B. Geohegan, G. Duscher, *ACS nano* **2015**, *9*, 10482.

[184]   A. Godoy Junior, A. Pereira, M. Gomes, M. Fraga, R. Pessoa, D. Leite, G. Petraconi, A. Nogueira, H. Wender, W. Miyakawa, M. Massi, A. da Silva Sobrinho, *Catalysts* **2020**, *10*, 282.

[185]   A. P. Singh, N. Kodan, B. R. Mehta, A. Dey, S. Krishnamurthy, *Materials Research Bulletin* **2016**, *76*, 284.

[186]   J. Liang, N. Wang, Q. Zhang, B. Liu, X. Kong, C. Wei, D. Zhang, B. Yan, Y. Zhao, X. Zhang, *Nano Energy* **2017**, *42*, 151.

[187]   D. Berends, D. H. Taffa, H. Meddeb, P. Schwager, K. Gehrke, M. Vehse, C. Agert, *Advanced Photonics Research* **2023**, https://onlinelibrary.wiley.com/doi/pdf/10.1002/adpr.202300163.

[188]   X. Lü, A. Chen, Y. Luo, P. Lu, Y. Dai, E. Enriquez, P. Dowden, H. Xu, P. G. Kotula, A. K. Azad, D. A. Yarotski, R. P. Prasankumar, A. J. Taylor, J. D. Thompson, Q. Jia, *Nano letters* **2016**, *16*, 5751.

[189] B. Xu, H. Y. Sohn, Y. Mohassab, Y. Lan, *RSC Advances* **2016**, *6*, 79706.

[190] H. W. S. Barros, D. A. Duarte, J. C. Sagás, *Thin Solid Films* **2020**, *696*.

[191] R. Shi, Y. Zhu, M. Li, X. Wu, Y. Ji, N. Yang, R. Jiang, Z. Lei, Z. Liu, J. Sun, *ACS Appl. Nano Mater.* **2023**, *6*, 15266.

[192] R. Alipour Moghadam Esfahani, S. K. Vankova, A. H. Monteverde Videla, S. Specchia, *Applied Catalysis B: Environmental* **2017**, *201*, 419.

[193] S. V. Ovsyannikov, X. Wu, V. V. Shchennikov, A. E. Karkin, N. Dubrovinskaia, G. Garbarino, L. Dubrovinsky, *Journal of physics. Condensed matter an Institute of Physics journal* **2010**, *22*, 375402.

[194] P. Sun, X. Hu, G. Wei, R. Wang, Q. Wang, H. Wang, X. Wang, *Applied Surface Science* **2021**, *548*, 149269.

[195] H. J. Liu, M. Q. Luo, L. X. Yang, C. L. Zeng, C. Fu, *Ceramics International* **2022**, *48*, 25538.

[196] S.-S. Huang, Y.-H. Lin, W. Chuang, P.-S. Shao, C.-H. Chuang, J.-F. Lee, M.-L. Lu, Y.-T. Weng, N.-L. Wu, *ACS Sustainable Chem. Eng.* **2018**, *6*, 3162.

[197] Y. Cho, S. Kim, B. Park, C.-L. Lee, J. K. Kim, K.-S. Lee, I. Y. Choi, J. K. Kim, K. Zhang, S. H. Oh, J. H. Park, *Nano letters* **2018**, *18*, 4257.

[198] C. Wu, Z. Gao, S. Gao, Q. Wang, H. Xu, Z. Wang, B. Huang, Y. Dai, *Journal of Energy Chemistry* **2016**, *25*, 726.

[199] E. Wierzbicka, E. Szaniawska-Białas, T. Schultz, A. O. Basilio, D. Siemiaszko, K. Ray, N. Koch, N. Pinna, M. Polański, *ChemSusChem* **2024**.

[200] Z. Zhang, M. N. Hedhili, H. Zhu, P. Wang, *Physical chemistry chemical physics PCCP* **2013**, *15*, 15637.

8.   List of Publications

8.1 Publications in Peer-Reviewed Journals as first Author

1. Berends, Dennis; Schwager, Patrick; Gehrke, Kai; Vehse, Martin; Agert, Carsten (2022): Effect of asymmetric power distribution in bipolar reactive sputtering on the optoelectronic and microstructure properties of titanium dioxide for solar water splitting. In: *Vacuum* 203, S. 111290. DOI: 10.1016/j.vacuum.2022.111290

2. Berends, Dennis; Taffa, Dereje H.; Meddeb, Hosni; Schwager, Patrick; Gehrke, Kai; Vehse, Martin; Agert, Carsten (2023): Precise Control of Broadband Light Absorption and Density of Ti^{3+} States in Sputtered Black TiO_2 Thin Films. In: *Advanced Photonics Research* 4 (10), 2300163, S. 2300163. DOI: 10.1002/adpr.202300163

3. Berends, Dennis; Schwager, Patrick; Gehrke, Kai; Vehse, Martin; Agert, Carsten (2024): Precise Control of Broadband Light Absorption and Density of Ti^{3+} States in Sputtered Black TiO_2 Thin Films. In: *ACS Omega* 2024, 9, 13, 15251-15258. DOI: 10.1021/acsomega.3c09772

8.2 Publications in Peer-Reviewed Journals as Co-Author

1. Osterthun, Norbert; Helamieh, Mark; Berends, Dennis; Neugebohrn, Nils; Gehrke, Kai; Vehse, Martin; Kerner, Martin; Agert, Carsten (2021): Influence of spectrally selective solar cells on microalgae growth in photo-bioreactors. In: *AIP Conf. Proc.* 2361 (1), S. 70001. DOI: 10.1063/5.0054814.

2. Götz-Köhler, Maximilian; Banik, Udayan; Meddeb, Hosni; Neugebohrn, Nils; Berends, Dennis; Gehrke, Kai; Vehse, Martin; Agert, Carsten (2022): Switchable photovoltaic window for on-demand shading and electricity generation. In: *Solar Energy* 232, S. 433–443. DOI: 10.1016/j.solener.2021.12.071.

3. Meddeb, Hosni; Götz-Köhler, Maximilian; Neugebohrn, Nils; Banik, Udayan; Osterthun, Norbert; Sergeev, Oleg; Berends, Dennis; Lattyak, Colleen; Gehrke, Kai; Vehse, Martin (2022): Tunable Photovoltaics: Adapting Solar Cell Technologies to Versatile Applications. In: *Advanced Energy Materials* 12 (28), 2200713, S. 2200713. DOI: 10.1002/aenm.202200713.

4. Osterthun, Norbert; Meddeb, Hosni; Berends, Dennis; Neugebohrn, Nils; Gehrke, Kai; Vehse, Martin; Agert, Carsten (2022): Titanium-Oxide-Based Electron-Selective Contact for Ultrathin Germanium Quantum Well Solar Cell. In: *Phys. Status Solidi A* 219 (21), Artikel 2200292, S. 2200292. DOI: 10.1002/pssa.202200292.

5. Banik, Udayan; Meddeb, Hosni; Berends, Dennis; Reininghaus, Nies; Sergeev, Oleg; Busch, Luisa; Gehrke, Kai; Vehse, Martin; Agert, Carsten (2024): Impact of parasitic heat fluxes on deep sub-ambient radiative coolers under variable pressure. In: *Applied Thermal Engineering* 237, S. 121655. DOI: 10.1016/j.applthermaleng.2023.121655.

8.3 Other Scientific Contributions

1. E-MRS Fall 2022 (poster presentation)
2. ICTF 2023 (poster presentation)

9. Curriculum Vitae

9.1 Education

Carl von Ossietzky University Oldenburg   Oldenburg, Germany
Doctoral Degree (Dr. rer. nat., Physics)   10.2019 –

Carl von Ossietzky University Oldenburg   Oldenburg, Germany
Master of Science (Physics)   10.2015 – 12.2018

Carl von Ossietzky University Oldenburg   Oldenburg, Germany
Bachelor of Science (Physics/Mathematics)   10.2011 – 10.2015

Teletta-Groß-Gymnasium Leer   Leer, Germany
Abitur (Allgemeine Hochschulreife)   06.2011

9.2 Research and Work

DLR Institute of Networked Energy Systems   Oldenburg, Germany
Research Assistant and Guest Researcher   01.2019 –

Next Energy   Oldenburg, Germany
Student Research Assistant   04.2017 – 12.2018

MTA EK MFA – Institute of Technical Physics and Material Science

Budapest, Hungary
ERASMUS Internship   01.2015 – 08.2015

Erklärung der Eigenständigkeit

Hiermit erkläre ich, dass ich die vorliegende Dissertation selbstständig verfasst und nur die angegebenen Hilfsmittel benutzt habe. Die Arbeit wurde weder in ihrer Gesamtheit noch in Teilen einer anderen wissenschaftlichen Hochschule zur Begutachtung in einem Promotionsverfahren vorgelegt. Die Leitlinien guter wissenschaftlicher Praxis an der Carl von Ossietzky Universität Oldenburg wurden befolgt. Außerdem wurden im Zusammenhang mit dem Promotionsvorhaben keine kommerziellen Vermittlungs- oder Beratungsdienste (Promotionsberatung) in Anspruch genommen.

Oldenburg, den

_____

Dennis Berends

Danksagung

Time, what is time? frage ich mich, während ich hier nun in den finalen Zügen meiner Doktorarbeit sitze und die letzten Jahre im Kopf Revue passieren lasse. So viele schöne Erinnerungen und Freundschaften sind entstanden, so viel Zeit ist vergangen. An dieser Stelle möchte ich mir nun einen Moment nehmen, all denen zu danken, die dazu beigetragen haben, dass ich hier sitzen kann und nicht unterwegs im Strudel der Zeit untergegangen bin.

Zunächst möchte ich mich bei Herrn Professor Agert bedanken, der mir die Möglichkeit gegeben hat, am Deutschen Zentrum für Luft- und Raumfahrt und an der Universität Oldenburg zu promovieren. In den persönlichen Treffen und Seminaren fand stets ein konstruktiver Austausch statt und die inspirierenden Anregungen und kritischen Nachfragen haben die Arbeit zu dem gemacht, was sie letztendlich geworden ist. Herrn Professor Wark danke ich für den guten fachlichen Austausch und dafür, dass er sich bereit erklärt hat, meine Dissertation als Zweitgutachter zu betreuen.

Mein Dank gilt auch Martin Vehse und Kai Gehrke, die diese Promotion von der ersten Minute an begleitet haben und immer zur Stelle waren, wenn Probleme auftauchten und durch fachliche Diskussionen den wissenschaftlichen Mehrwert der Arbeit deutlich erhöht haben. Danke, dass ihr so entspannte Abteilungs- und Gruppenleiter seid.

Mein besonderer Dank gilt Patrick Schwager, der sich sehr viel Zeit genommen hat und mir in jeder Hinsicht mit Rat und Tat zur Seite stand. Insbesondere die wöchentlichen Treffen haben dazu beigetragen, die Arbeit in geordnete Bahnen zu lenken, und ohne die zahlreichen Iterationen der verschiedenen Manuskripte hätte die Promotion wesentlich mehr Zeit in Anspruch genommen.

Natürlich möchte ich mich auch bei all meinen Kollegen des Instituts für Vernetzte Energiesysteme bedanken. Es war eine großartige Zeit mit euch. Der Zusammenhalt in der Gruppe war fantastisch, immer war jemand bereit zu helfen und so sind die letzten Jahre wie im Flug vergangen. Besonders hervorheben möchte ich unser Doktorandenzimmer mit Norbert Osterthun, Maximilian Götz-Köhler, Udayan Banik und Colleen Lattyak, die nicht nur durch die gemeinsame (Leidens-)Zeit sehr gute Freunde geworden sind. Weiterhin möchte ich mich bei Claas Koch, Oleg Sergeev, sowie Martin Kellermann und dem restlichen OBM bedanken, die durch ihre tatkräftige Arbeit nicht nur das Technikum und die Geräte in Schuss gehalten haben, sondern auch bei Problemen sofort mit ihrem Fachwissen zur Verfügung standen und somit zeitliche Verzögerungen auf ein Minimum reduziert haben.

Mein größter Dank gilt meinen Eltern, meinen Geschwistern, meinen Freunden (insbesondere der CLP-Runde) und meiner Freundin Lina. Nur durch eure Unterstützung bin ich so weit gekommen. Ihr habt mir immer Mut gemacht und mich motiviert, so dass meine Promotion zu einer wunderbaren Zeit wurde, die ich nie vergessen werde und an die ich mich gerne erinnere.